J Adv Ceram

Research Article

Dense core–shell eutectic Zr–Ta–O as a sacrificial layer of YSZ topcoat for enhanced CMAS resistance via dynamic sealing and self-removal

Jun-Hui Luo[1,2], Gang Yan[1,2], Guang-Nan Xu[1,2,✉], Chang-Xing Zhang[1,2], Ke Cao[1,2,✉], Jun-Kai Liu[1,2], Yi-Chun Zhou[1,2], Li Yang[1,2,✉]

Cite this article: Luo J-H, Yan G, Xu G-N, et al. *J Adv Ceram* 2026, **15**(6): 9221300. https://doi.org/10.26599/JAC.2026.9221300

ABSTRACT: Thermal barrier coatings (TBCs) are critical in protecting hot-section components. A double-layered TBC system comprising a eutectic Zr–Ta–O (ZTO) core–shell structured top layer and a yttria-stabilized zirconia (YSZ) underlayer was fabricated via atmospheric plasma spraying (APS). This study systematically investigates its mechanical properties and corrosion resistance under calcium–magnesium–aluminosilicate (CMAS, CaO–MgO–Al_2O_3–SiO_2) attack. The results demonstrate that the eutectic microstructure exhibits exceptional plastic deformability, achieving a compressive strain of more than 30% and a yield strength of up to 4.5 GPa through *in situ* mechanical testing. The dense Zr–Ta–O layer effectively seals CMAS infiltration through eutectic solidification-induced densification. Simultaneously, it functions as a sacrificial layer where phase transformation and thermal expansion mismatch induce strain, triggering spallation of corrosion products to protect the underlying YSZ. Finite element simulations quantitatively reveal the distribution of interfacial stress fields governing CMAS-driven crack propagation at the top layer. This design paradigm provides new insights into CMAS-resistant eutectic TBC architectures.

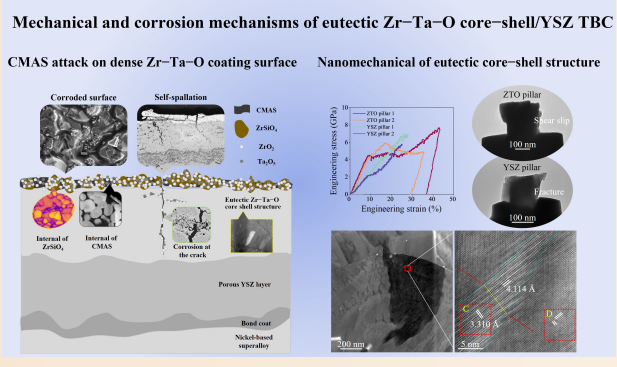

KEYWORDS: eutectic core–shell structure; double-layered thermal barrier coatings (TBC); calcium–magnesium–aluminosilicate corrosion resistance; *in situ* mechanics; finite element simulation

1 Introduction

As aeroengine design evolves for enhanced maneuverability and efficiency, turbine inlet temperatures now routinely exceed 1800 °C [1,2], imposing unprecedented challenges on blade cooling systems. Despite the extreme-temperature capabilities of advanced Ni-based superalloys, thermal barrier coatings (TBCs) remain indispensable for further reducing surface operating temperatures [3,4]. Serving under extreme conditions—including high-velocity hot gas erosion, thermal shock, foreign object damage, and calcium–magnesium–aluminosilicate (CMAS, CaO–MgO–Al_2O_3–SiO_2) corrosion [4]—TBCs face multifaceted degradation threats. CMAS corrosion, originating from atmospheric dust, sand, volcanic ash, and ingested particulates during engine transients, has become critical in next-generation engines, inducing severe coating spallation through thermomechanical stresses from rapid cooling [5].

CMAS corrosion degradation proceeds via two synergistically coupled mechanisms governing the corrosion morphology evolution: (i) pore filling-induced thermomechanical stress due to the coefficient of thermal expansion (CTE) mismatch, and (ii) thermochemically driven phase transformations [6]. Thermal-mechanical degradation and thermal-chemical corrosion under CMAS corrosion compromise conventional yttria-stabilized zirconia (YSZ) TBCs, as CMAS infiltration promotes selective yttrium dissolution. This triggers detrimental tetragonal to monoclinic (t → m) phase transformations, where the associated volumetric expansion (3%–5%) induces stress concentration. Subsequent microcrack propagation ultimately causes catastrophic delamination [7]. Consequently, developing TBCs with enhanced CMAS resistance and mechanical robustness is imperative.

Current CMAS-resistant strategies include (i) compositional modification (e.g., $YO_{1.5}$/$TaO_{2.5}$ codoped ZrO_2) enabling rare earth (RE)-CMAS reactive crystallization to form dense infiltration-block phases [8,9]; (ii) surface engineering via laser texturing or

[1] School of Advanced Materials and Nanotechnology, Xidian University, Xi'an 710126, China. [2] Shaanxi Key Laboratory of High-Orbits-Electron Materials and Protection Technology for Aerospace, Xidian University, Xi'an 710126, China.

✉ Corresponding authors. E-mail: G.-N. Xu, xuguangnan@xidian.edu.cn; K. Cao, caoke@xidian.edu.cn; L. Yang, lyang-xd@xidian.edu.cn

Received: January 6, 2026; Revised: March 23, 2026; Accepted: April 13, 2026

Al_2O_3 overlays to reduce wettability or form dense protective reaction layers [10] (e.g., $ZrSiO_4$, a stable compound under thermal shock and with comparable thermodynamic properties to those of YSZ [11]); and (iii) alternative material systems such as rare-earth zirconates [12], rare-earth tantalates [13,14], rare-earth phosphates [15], and high-entropy oxides [16,17]. These strategies aim to reduce CMAS adhesion/infiltration and enhance corrosion resistance, yet critical limitations persist: Capillary-driven CMAS penetration in porous coatings precedes dense RE-CMAS barrier formation (e.g., apatite crystallization in doped zirconates [8,12]); surface barriers suffer poor strain tolerance from CTE mismatch-induced delamination; laser modifications generate post-treatment cracks due to rapid solidification stresses [10]; dense vertically cracked YSZ offers strain accommodation; and novel materials lack sufficient toughness for long-term service. Crucially, existing approaches passively block infiltration but lack active sacrificial mechanisms to expel corrosion products. Recent functionally stratified designs—such as bilayer/multilayer coatings or multiphase monolayers—show promise in overcoming the service-life limitations of conventional 7–8YSZ TBCs [1]. Coating performance enhancement ultimately requires rational optimization of functionally graded architectures.

Recent studies have revealed that entropy-stabilized high-entropy oxide $A_6B_2O_{17}$ (A = Hf, Zr; B = Ta, Nb) superstructures—exhibiting a configurational entropy of 4.50R (where R is the gas constant, 8.314 $J{\cdot}mol^{-1}{\cdot}K^{-1}$) from cation disorder [18]—demonstrate exceptional high-temperature stability (to 2250 °C) [19,20], favorable thermal expansion (10.9×10^{-6} $°C^{-1}$ at 1200 °C) [21], low thermal conductivity (1.0 $W{\cdot}m^{-1}{\cdot}K^{-1}$ at 1000 °C) [22], and high-temperature chemical stability [23]. The $Zr_6Ta_2O_{17}$ coating shows superior fracture toughness versus YSZ (3.8 vs. ~2.7 $MPa{\cdot}m^{1/2}$) and withstands 2000 thermal cycles at 1150 °C [7,24]. Combined with outstanding CMAS corrosion resistance in bulk [6,25,26] and Na_2SO_4–V_2O_5 salt resistance in coatings [27], this system emerges as a promising next-generation TBC candidate. Eutectic A–B–O compounds based on $A_6B_2O_{17}$ exhibit superior thermophysical and mechanical properties compared with pure components [28,29]. The Ta–$Hf_6Ta_2O_{17}$ eutectic achieves simultaneous strength–toughness enhancement (4.21±0.09 $MPa{\cdot}m^{1/2}$) through intrinsic interfacial strength and crack deflection [30], while Ta_2O_5 contributes to a high melting point (1800 °C), toughness, and corrosion resistance [31]. $Hf_6Ta_2O_{17}$/Ta_2O_5 forms a dense three-dimensional (3D) $Hf_6Ta_2O_{17}$/Ta_2O_5 hypereutectic oxide scale for oxidation resistance [19,32]. Our prior work confirmed that atmospheric plasma spraying (APS)-sprayed $Zr_6Ta_2O_{17}$ coatings maintain oxidation resistance and thermal cycling life independent of the initial Ta_2O_5 content [7]. Excess HfO_2 in ceramic blocks enhances density and reacts with CMAS to form dense protective $HfSiO_4$, mitigating penetration and corrosion [6,25]. The APS parameter enables decomposition-regulated formation of dense eutectic $Hf_6Ta_2O_{17}$ TBC on Ni alloys [33,34] that facilitated by vapor pressure differential-induced Ta_2O_5/HfO_2 segregation [28]. Nevertheless, the microstructural characteristics and service behavior of A–B–O eutectic TBC remain underexplored, making CMAS corrosion resistance pivotal for leveraging its excellent mechanical properties in practical applications.

Despite inherent material degradation limits, coating optimization persistently seeks to delay failure. We propose a novel bilayer thermal barrier coating system comprising a sacrificial Zr–Ta–O (ZTO) eutectic topcoat over a YSZ underlayer fabricated via APS. This design synergistically integrates the favorable thermomechanical properties and CMAS resistance of $Zr_6Ta_2O_{17}$ with the low thermal conductivity and thermal shock resistance of YSZ. The architecture features a dense multiphase eutectic top layer above a porous underlayer, leveraging (i) eutectic densification during APS solidification to seal initial CMAS infiltration; (ii) active ZrO_2–SiO_2 reactions forming zircon ($ZrSiO_4$) barriers that immobilize molten CMAS; (iii) lattice mismatch-induced spallation enabling self-removal of damaged zones under thermal cycling. To our knowledge, this represents the first demonstration of sacrificial protection in eutectic TBCs.

In this study, APS-fabricated core–shell structured ZTO/8YSZ coatings were systematically investigated. *In situ* nanomechanical methods evaluated the mechanical properties of oxidized eutectic topcoats, while transmission electron microscopy (TEM) and transmission electron backscatter diffraction (EBSD-TKD) elucidated nanoscale CMAS corrosion mechanisms and microstructural evolution at 1250 °C. Finite element analysis simulated coating spallation stresses, providing comprehensive insights into the degradation behavior of this dual-layer system. This approach addresses the corrosion vulnerabilities of conventional YSZ while clarifying A–B–O eutectic microstructure–property relationships.

2 Experiment and simulation

2.1 Preparation of core–shell structured eutectic ZTO/8YSZ double-layer TBCs

Commercial-grade 8 wt% yttria-stabilized zirconia (8YSZ), ZrO_2, and Ta_2O_5 powders (≥ 99.99% purity, China New Metal Materials Technology Co., Ltd.) were wet-milled at 100 $r{\cdot}min^{-1}$ for 8 h in alcohol using zirconia balls (86 mol% ZrO_2 : 14 mol% Ta_2O_5). The slurry was calcined at 1600 °C for 8 h to synthesize the orthorhombic $Zr_6Ta_2O_{17}$ (o-$Zr_6Ta_2O_{17}$) precursor, followed by ball milling and sieving (~6.5 μm). Densification via spray granulation (inlet/outlet temperatures: 250/100 °C) yielded spherical $Zr_6Ta_2O_{17}$ powder, with 8YSZ prepared identically. GH536 Ni-based superalloy substrates were grit-blasted (500–600 μm alumina, 0.6 MPa) to enhance adhesion. A NiCrAlY bond coat was deposited by high-velocity oxygen-fuel (HVOF) spraying, followed by APS of ZTO/8YSZ bilayer coatings. The spraying parameters are listed in Table 1. To ensure complete phase formation, as-sprayed ZTO/8YSZ coatings underwent post-deposition oxidation at 950 °C for 4 h until achieving a characteristic white coloration. Additional methodology details are reported elsewhere [27].

2.2 *In situ* mechanical tests of core–shell structured eutectic Zr–Ta–O

The mechanical properties of the top coat were evaluated through *in situ* transmission electron microscope (TEM; Talos F200X G2). Focused ion beam (FIB)-milled square nanopillars with an average height of 349±11 nm and an average width of 146±6 nm were lifted out from the top coat, mounted on molybdenum half-grids, and then compressed using a 1 μm diamond flat punch at a displacement rate of 2 $nm{\cdot}s^{-1}$ by PicoIndenter 95. To evaluate the mechanical properties of the eutectic core–shell structure, nanopillar compression tests were performed on a YSZ bulk with identical pillar dimensions [35]. High-speed imaging captured the deformation sequence concurrently with load–displacement data acquisition with an exposure time of 25 ms per frame. The engineering stress was calculated by dividing the load by the cross-sectional area at mid-pillar height.

2.3 CMAS corrosion experiment

A synthetic CMAS deposit (33CaO–9MgO–13Al_2O_3–45SiO_2,

Table 1 Spraying parameters of bond coat and ceramic layers

Layer	Spraying distance (mm)	Powder feeding rate (g·min^{-1})	Fuel flow (L·min^{-1})	Oxygen gas flow (L·min^{-1})	Air flow (L·min^{-1})	Spraying power (kW)	Substrate temperature (°C)
8YSZ	110	20	40	10	35	40	200
ZTO	110	20	40	10	28	40	200

mol%) simulating volcanic ash was prepared from ≥ 99.9% pure oxides. Stoichiometrically weighed powders were homogenized in ethanol via planetary ball milling (400 r·min^{-1}, 4 h), dried at 100 °C, and vitrified by calcining at 1300 °C for 4 h. The resulting amorphous CMAS was ground and sieved (< 75 μm) and then suspended in anhydrous ethanol to form a slurry. This was uniformly applied onto coatings, with the deposited amount maintained at 10±1 mg·cm^{-2} (gravimetrically verified) after drying at 80 °C. Isothermal corrosion tests at 1250 °C employed heating/cooling rates of 10 °C·min^{-1}, with exposure durations of 0.5, 1, 2, 5, and 8 h to assess time-dependent degradation.

2.4 Microstructure characterization

Cross-sectional samples of coatings were sectioned perpendicular to the interface using a diamond wire cutter (ϕ0.25 mm wire). Samples were epoxy-mounted in conductive resin and then progressively ground and polished with diamond lapping film (30–0.5 μm) under water lubrication. Final surface finishing employed vibratory polishing with 0.05 μm diamond suspension for 4 h to minimize preparation artifacts. Samples were sputter-coated with ~10 nm Au (10 kV, 60 s) to enhance conductivity.

The coating morphology, CMAS corrosion features, penetration depth, and elemental redistribution were characterized using a FIB–SEM (Helios 5 CX) with an energy-dispersive X-ray spectrometer (EDS; Ultim Max) and a transmission electron backscatter diffractometer (TKD; C-Nano). Coating porosity was quantified from backscattered electron-scanning electron microscopy (BSE-SEM) images via ImageJ software. Site-specific TEM lamellae (< 100 nm thickness) were extracted from critical regions: (i) CMAS infiltration regions, (ii) unaffected coating zones, and (iii) coating/substrate interfaces at several corrosion intervals (0.5–8 h). Lamellae were plasma-cleaned (H_2/O_2, 40 W for 2 min) before TEM analysis at 200 kV with EDS (Super-X) for phase evolution assessment. TKD mapping at 30 kV further resolved the phase distribution along corrosion penetration paths.

2.5 CMAS penetrant corrosion deformation theory

A finite element model simulated CMAS corrosion-induced deformation in bilayer coatings, covering CMAS penetration, coating dissolution, tetragonal-to-monoclinic phase transformation, and thermal shrinkage. Key assumptions: (i) The CMAS-corroded regions at high temperatures are assumed to be in a stress-free state due to stress relaxation; (ii) the stabilizing element in the ceramic regions completely dissolved by CMAS is assumed to be fully depleted and incorporated into the CMAS melt.

The thermal loading process is divided into two stages: an isothermal corrosion stage and a cooling stage. During the high-temperature stage, CMAS infiltration and coating dissolution occur, whereas during the cooling stage, phase transformation and associated deformation occur.

The governing equation of CMAS penetration is written as Eq. (1) [36]:

$$\dot{c}_i = D\nabla^2 c_i \tag{1}$$

where c_i denotes the molar concentration of element *i*. *i* is numbered from 1 to 4 and represents Ca, Mg, Al, and Si, respectively. D represents the diffusion coefficient of CMAS in the coating domain.

The governing equation of coating dissolution corrosion is given by Eq. (2) [36]:

$$\dot{n} = \zeta(1 - n - f_0)\rho_{\mathrm{CMAS}} + \beta\nabla^2 n$$

with

$$\begin{aligned}\rho_{\mathrm{CMAS}}(c_i) &= M_{\mathrm{CaO}} \cdot c_1 + M_{\mathrm{MgO}} \cdot c_2 + M_{\mathrm{Al_2O_3}} \cdot c_3/2 + M_{\mathrm{SiO_2}} \cdot c_4 \\ &= \sum_{i=1}^{4} M_i c_i\end{aligned} \tag{2}$$

where n is the degree of coating corrosion dissolution; ζ is the proportional coefficient; ρ_{CMAS} is the mass density of CMAS; f_0 is the coating porosity. M_{CaO}, M_{MgO}, $M_{\mathrm{Al_2O_3}}$, and $M_{\mathrm{SiO_2}}$ denote the molar masses of CaO, MgO, Al_2O_3, and SiO_2, respectively. The gradient term describes the corroded and uncorroded domain interface and β denotes the gradient term coefficient.

Based on the second assumption, the interdiffusion of elements between the coating and molten CMAS destabilizes tetragonal ZrO_2 during cooling. This diffusion-controlled process triggers a complete transformation to the monoclinic phase upon reaching the critical tetragonal-to-monoclinic transition temperature of ZrO_2. The volume fraction of the phase-transformation region in the fully corroded zone is defined as η. The governing equation for this phase transformation is shown in Eq. (3):

$$\eta = H(T_c - T) \text{ with } H(x) = \begin{cases} 0, & x < 0 \\ 1, & x \geq 0 \end{cases} \tag{3}$$

where H denotes the Heaviside function, T_c represents the metastable equilibrium temperature of ZrO_2, and T is the system temperature. The governing equation of coating deformation is given by Eqs. (4) and (5) [36]:

$$\varepsilon = (\sigma - \lambda tr\sigma \boldsymbol{I}/(2G + 3\lambda))/2G + \alpha(T - T_0)\boldsymbol{I} + \chi\eta n\boldsymbol{I} \tag{4}$$

$$\nabla \cdot \sigma = 0 \tag{5}$$

where $\boldsymbol{\sigma}$ and $\boldsymbol{\varepsilon}$ represent the stress and strain tensors, respectively. λ, G, α, and $\boldsymbol{I}$ denote the Lamé constants, shear modulus, coefficient of thermal expansion, and unit tensor, respectively. χ is a proportionality constant. The terms on the right-hand side of Eq. (4) represent the elastic strain, thermal strain, and transformation strain, respectively. T_0 is the initial temperature of the system.

To represent the influence of CMAS penetrating corrosion on the thermal expansion deformation of the coating, we express the coefficient of thermal expansion as a linear interpolation function of the degree of corrosion dissolution using Eq. (6):

$$\alpha = \alpha_0(\boldsymbol{I} - f_0 - n) + \alpha_1 n \tag{6}$$

The CMAS penetration corrosion process only occurs in the ceramic layer. α_0 and α_1 denote the coefficients of thermal

expansion of original material and completely corroded material. Table 2 gives the simulation parameters applied in the model. All control equations are calculated using the general form partial differential equation module in COMSOL.

At the initial stage, all field variables are set to zero. The bottom boundary of the coating is fully constrained, with all displacement components fixed to zero. After the isothermal corrosion stage, the temperature during the cooling stage is controlled as Eq. (7):

$$T = \begin{cases} T_0, & \text{at high-temperature stage} \\ T_0 - k_m - t, & \text{at cooling stage} \end{cases} \quad (7)$$

where t denotes the time at the cooling stage, and k_m is a cooling rate constant.

3 Results

3.1 Sacrificial layer microstructure for blocking CMAS penetration

Figure 1 shows cross-section BSE-SEM images of the as-deposited ZTO/8YSZ bilayer coatings, with the interfaces marked by yellow dotted lines. The total coating thickness is 433±25 μm, comprising

Table 2 Simulation parameters applied in model

λ_{ZrTaO} (GPa)	G_{ZrTaO} (GPa)	α^0_{ZrTaO} (K^{-1})	α^1_{ZrTaO} (K^{-1})	D_{ZrTaO} ($m^2 \cdot s^{-1}$)	ζ_{ZrTaO} ($m^3 \cdot kg^{-1} \cdot s^{-1}$)	β_{ZrTaO} ($J \cdot m^{-1}$)
1.15	0.769	10×10^{-6}	8.1×10^{-6} [37]	8.84×10^{-15}	1.9×10^{-8} [36]	1×10^{-3}
λ_{YSZ} (GPa)	G_{YSZ} (GPa)	α^0_{YSZ} (K^{-1})	α^1_{YSZ} (K^{-1})	D_{YSZ} ($m^2 \cdot s^{-1}$)	ζ_{YSZ} ($m^3 \cdot kg^{-1} \cdot s^{-1}$)	β_{YSZ} ($J \cdot m^{-1}$)
8.65	5.77	11×10^{-6} [37]	8.1×10^{-6} [37]	8.84×10^{-13} [36]	1.9×10^{-8} [36]	1×10^{-3}
λ_{SUB} (GPa)	G_{SUB} (GPa)	α_{SUB} (K^{-1})	χ	T_c (°C)	T_0 (°C)	—
103.9 [37]	69 [37]	14×10^{-6} [37]	0.01 [38]	1000 [39]	1250	—

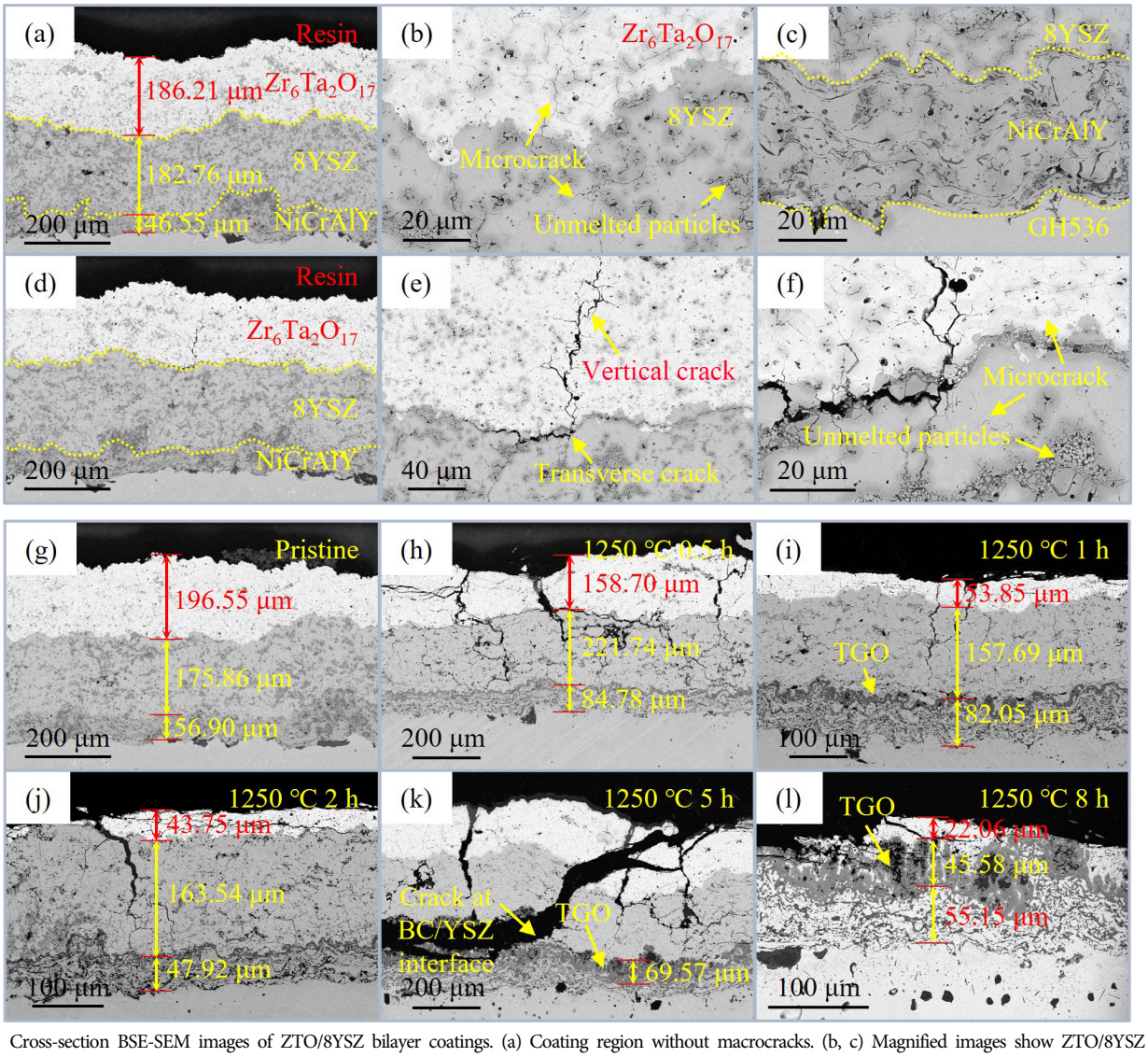

Fig. 1 Cross-section BSE-SEM images of ZTO/8YSZ bilayer coatings. (a) Coating region without macrocracks. (b, c) Magnified images show ZTO/8YSZ and 8YSZ/NiCrAlY/GH536 interfaces. (d) Coating region with macrocracks. (e, f) Magnified images show vertical crack in Zr–Ta–O layer and transverse crack at ZTO/8YSZ interface. (g–l) CMAS corrosion at 1250 °C for 0, 0.5, 1, 2, 5, and 8 h.

a 181±17 μm Zr–Ta–O top layer and a 192±21 μm 8YSZ intermediate layer on a NiCrAlY bond coat (61±22 μm) adhered to a GH536 superalloy substrate. High-magnification images (Figs. 1(b) and 1(c)) reveal the characteristic lamellar microstructure with 2.0%±0.8% porosity in the compact Zr–Ta–O layer and 15.4%±3.9% porosity in the porous 8YSZ layer, where unmelted particles are dispersed throughout the layered structures.

Microcracks (< 10 μm) are uniformly dispersed near structural heterogeneities, induced by thermal stress concentration of coating shrinkage during rapid solidification. Residual stresses from the CTE mismatch at the ZTO/8YSZ interface promoted transverse cracks to nucleate at the boundary and vertical cracks to propagate exclusively within the Zr–Ta–O layer toward the surface with an average crack length of 198±36 μm (Figs. 1(d)–1(f)). These cracks exhibited densities of 1.0 cracks·mm^{-1} (vertical) and 4.1 cracks·mm^{-2} (transverse), enhancing the bilayer coating strain tolerance while serving as a preferential CMAS infiltration pathway.

Figures 1(g)–1(l) compare cross-section BSE-SEM images of ZTO/8YSZ bilayer coatings after 1250 °C CMAS corrosion for 0, 0.5, 1, 2, 5, and 8 h. Molten CMAS rapidly penetrated vertical cracks via capillary action, accelerating elemental diffusion in the top layer. Zr–Ta–O spallation intensified with exposure time due to residual stress-driven crack propagation. The vertical crack density obtained from the coating with only 0.5 h of CMAS attack was 3.2 cracks·mm^{-1}, which was 3.2 times that of the original coating (Fig. 1(h)). Vertical cracks with extensive branching propagate from the surface toward the bond coat, interacting with transverse cracks to increase crack dimensions. Before crack propagation to the bond coat, the thermally grown oxide (TGO) thickness remained less than 3 μm (Figs. 1(i) and 1(j)). After 5 h of corrosion, the crack propagated to the bond coat. Direct hot air exposure caused rapid TGO growth, reaching 43.5±17.8 μm at 5 h (Fig. 1(k)), and thickening to 60.2±12.2 μm at 8 h (Fig. 1(l)).

Despite spectral overlap between Ta $M_{\alpha1}$ (1.710 keV) and Si $K_{\alpha1}$ (1.740 keV) peaks (0.030 keV separation < 130 eV detector resolution), the BSE image exhibiting atomic number (Z) contrast confirms distinct spatial distributions of Ca, Mg, Al, and Si relative to the ZTO coating. Consequently, reconstructed spectra from the white rectangular regions (Fig. 2)—selected via the region of interest (ROI) method—unambiguously resolve the spatial distributions of Ta and Si. Quantitative EDS analysis thus confirms the absence of elemental overlap between these phases, demonstrating CMAS penetration along the vertical crack. In spalled regions (Fig. 1(k)), nonuniform TGO growth consists primarily of rapidly formed Cr_2O_3-based oxides due to prolonged high-temperature oxidation (Fig. 2(b)). No CMAS infiltration was observed at the 8YSZ/bond coat interface.

Figure 3 compares the surface morphology of the as-oxidized ZTO/8YSZ coating with that of the ZTO/8YSZ coating after CMAS corrosion. The oxidized coating exhibited white solidified microstructures with unmelted particles (1.4±0.6 μm) and microcracks (2.0±0.5 μm), as shown in Figs. 3(a)–3(c). After 5 h of CMAS exposure, significant surface degradation occurred: Cracks widened to 11.1±3.1 μm (Fig. S1 in the Electronic Supplementary Material (ESM)), while ridge-like Zr–Si oxide precipitates with a diameter of 18.5±7.3 μm (Fig. 3(j)) formed from black amorphous CMAS phases, as confirmed by EDS point analysis. By 8 h, the precipitates thickened to 22.4±9.2 μm (Fig. 3(k)), and the crack networks expanded to 12.0±3.1 μm (Figs. 3(g)–3(i)). EDS mapping (Fig. 4) reveals significant Zr/Ta segregation relative to the as-sprayed coating, with the interstitial spaces filled by CMAS. Extending corrosion to 8 h shows an expanded spatial distribution of Zr and Ta clusters. EDS point analysis across diverse microstructural features (Fig. S2 in the ESM) revealed elemental composition variations at specific locations, with the phases confirmed by the XRD analysis of the coating surface (Fig. S3 in the ESM). For example, nanoscale Zr–Ta oxide ($Zr_xTa_{1-x}O_3$) particles (white contrast in BSE), with a diameter of 1.4±3.1 μm (Fig. 3(l), fitted by lognormal distribution), appeared randomly on the black surface. The transition to ridge-like Zr–Si oxides ($ZrSiO_4$) indicates CMAS-induced dissolution and reprecipitation, whereas Zr–Ta particles suggest reactive element partitioning during thermochemical attack. This morphology evolution drives bond coat crack propagation and accelerated oxidation via residual stresses from thermal mismatch and nonuniform TGO growth.

3.2 Enhanced compressive performance via eutectic core–shell structure

APS-sprayed TBCs develop lamellar microstructures through sequential deposition and solidification on the substrate. $Zr_6Ta_2O_{17}$ feedstock decomposes under plasma heating, forming Zr–Ta–O eutectic compounds critical for coating performance. FIB-machined rectangular Zr–Ta–O nanopillars with consistent dimensions underwent near-uniaxial compression with a flat punch (Movies 1 and 2 in the ESM), enduring over 30% engineering strain without fracture (Figs. 5(a) and 5(b)), with slight differences in yield strength caused by different deformation modes. However, this represents a significant enhancement in the compressive performance of nanopillars compared with bulk YSZ with equivalent dimensions, where the YSZ nanopillars exhibited higher yield strength and lower elastic modulus but underwent brittle fracture with minimal plastic deformation (Figs. 5(c) and 5(d), Movies 3 and 4 in the ESM). Pillar 1 of ZTO exhibited gradual plastic deformation via shear slip with work hardening, while pillar 2 of ZTO underwent plastic yield after reaching yield strength (Fig. 5(b)), likely due to high shear stress concentration at the indenter contact.

The exceptional deformability is attributed to unique microstructural features. FIB–SEM serial sectioning tomography (Fig. 6; complete dynamic 3D reconstruction sequences in Movie 5 in the ESM (120 frames, ~7.5 nm·slice^{-1})) enabled comprehensive 3D architectural reconstruction. This provides conclusive spatial evidence of the Ta-rich phase forming a fully percolating encapsulating shell around the Zr-dominated core in all dimensions, thereby definitively substantiating the core–shell nature of this segregation-derived microstructure.

The as-oxidized Zr–Ta–O eutectic layer displayed spherical and elongated droplet-like microstructures within a lamellar framework (Figs. 7(a), 7(d), and 7(g)). Atomic-resolution high-angle annular dark-field (HAADF)-scanning TEM (STEM) (Figs. 7(b) and 7(e)) revealed coating decomposition after spraying with nanoscale orthorhombic Ta_2O_5 (o-Ta_2O_5) shells (3–13 nm in thickness) on tetragonal ZrO_2 (t-ZrO_2) cores due to Ta segregation (Figs. 7(g)–7(i)), forming coherent $(200)_o||(101)_t$, $[01\bar{1}]_o||[010]_t$ interfaces (Fig. 7(e)). Specifically, TEM–EDS elemental mapping (Figs. 7(g)–7(i)) combined with the line-scan profile (Fig. S4 in the ESM) collectively demonstrates a compositionally abrupt core–cell interface. It constitutes a core–shell configuration, reducing the Zr–Ta–O layer porosity to 2.0% (vs. 15.4% in 8YSZ), which exhibits denser microstructure characteristics, as mentioned in Section 3.1. Furthermore, the intragranular superstructure of t-ZrO_2(H) (H denoting compounds forming a homologous series) formation in t-ZrO_2

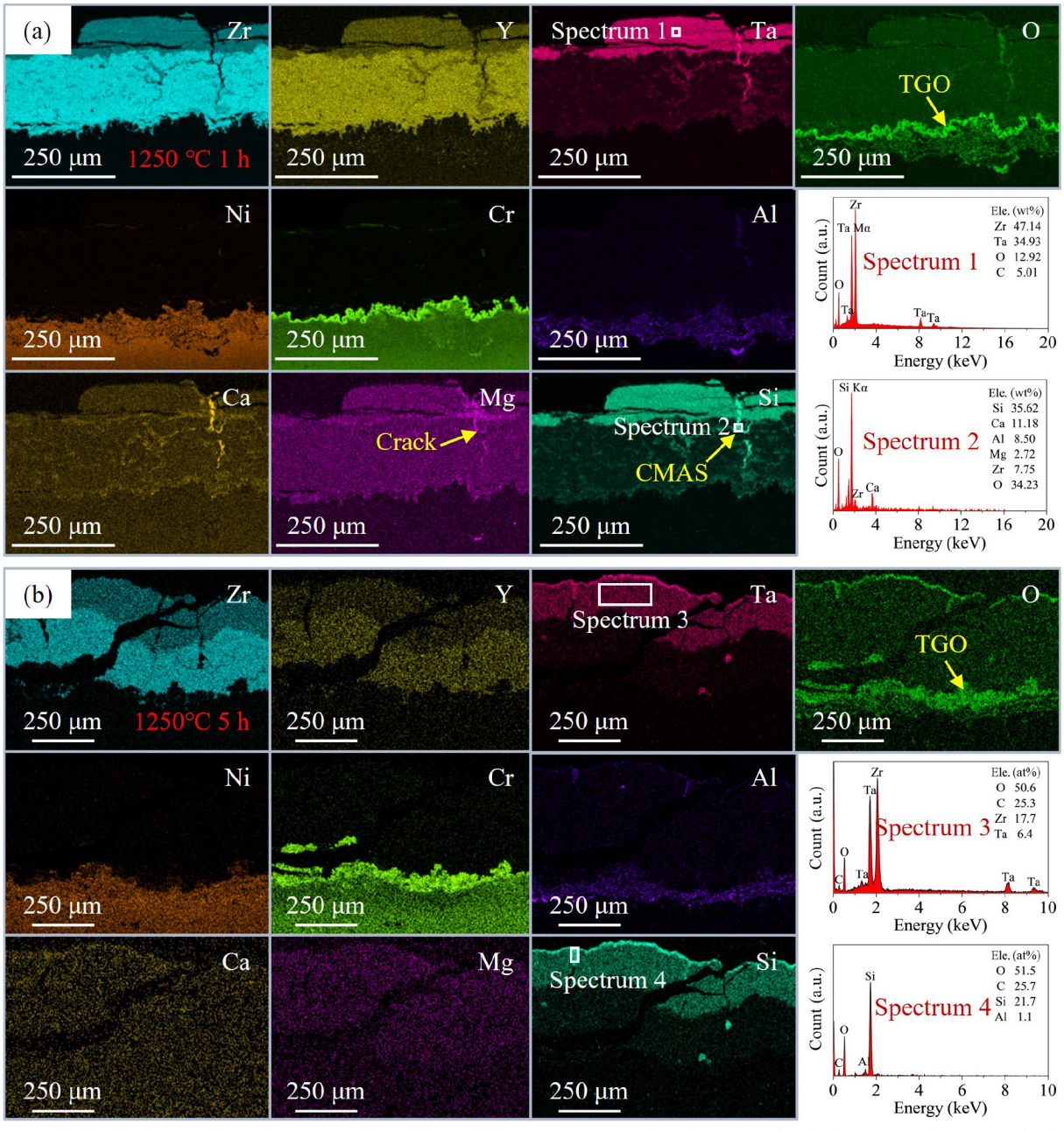

Fig. 2 Element distribution evolution during corrosive medium penetration process. (a) CMAS attack at 1250 °C for 1 h; (b) CMAS attack at 1250 °C for 5 h.

grains with the modulation vector $\boldsymbol{q} = 1/5\boldsymbol{a}^* + 3/5\boldsymbol{c}^*$ on $(010)_t$ (Figs. 7(a)–7(c), where $\boldsymbol{a}^*$ and $\boldsymbol{c}^*$ represent the reciprocal vectors of the lattice), as evidenced by the fast Fourier transform (FFT) satellite reflection of the superstructure marked by the red arrow in Fig. 7(f). Furthermore, TKD mapping confirmed alternating distributed $Zr_6Ta_2O_{17}$, ZrO_2, and Ta_2O_5 compounds within the layered coating (Figs. 8(a)–8(c)).

3.3 Sacrificial reaction mechanism: sealing, consuming, and self-spalling

Phase identification correlated EDS elemental mapping with microstructural features, with quantitative point analysis provided in Table 3. EDS quantitatively employed Zr-Lα, Ta-Mα, Y-Lα, O-Kα, Ca-Kα, Mg-Kα, Al-Kα, and Si-Kα lines (detector resolution ≤ 136 eV) to identify potential phases. The flat dark regions and protrusions in Fig. 3 correspond to amorphous CMAS, while ridge-like precipitates scattered in the amorphous CMAS are Zr–Si–O phases (primarily $ZrSiO_4$), and discrete white nanoparticles are Zr–Ta–O compounds (e.g., $Zr_xTa_{1-x}O_2$).

The detailed phase structure analysis of the topcoat was performed using EBSD-TKD on FIB-lifted TEM lamellae extracted from regions with different microstructural features, revealing significant degradation of the original coating surface caused by CMAS (Fig. 8). The as-oxidized Zr–Ta–O coating comprised layered-stacked orthogonal $Zr_6Ta_2O_{17}$ (50.7 vol%, *Ima*2, ICDD 04-025-3129), tetragonal ZrO_2 (29.5 vol%, $P4_2/nmc$), orthogonal Ta_2O_5 (13.7 vol%, *Pban*), cubic ZrO_2 (c-ZrO_2) (2.71 vol%, $Fm\bar{3}m$), and monoclinic ZrO_2 (m-ZrO_2) (0.38 vol%, $P2_1/c$) (Figs. 8(a)–8(c)). After the CMAS attack at 1250 °C for 8 h, TKD mapping of the TEM lamella extracted from the black flat CMAS area revealed numerous micron-scale spherical particles of m-ZrO_2 (49.8 vol%), incompletely decomposed o-$Zr_6Ta_2O_{17}$ (22.3 vol%), and a small amount of o-Ta_2O_5 (2.18 vol%), isolated and dispersed within the amorphous CMAS (25.2 vol%)

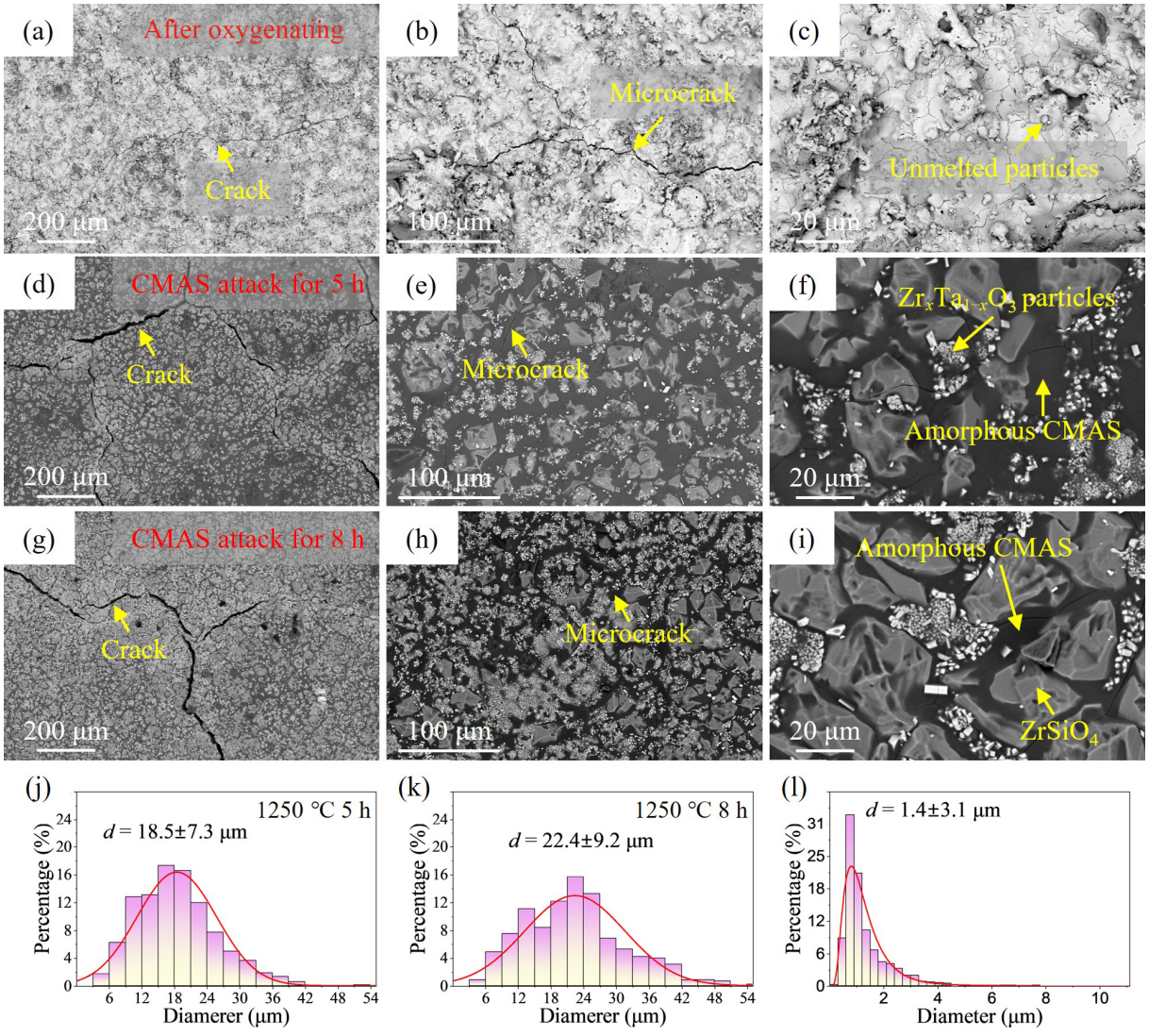

Fig. 3 Surface evolution under CMAS corrosion at 1250 °C: (a–d) As-oxidized ZTO/8YSZ with microcracks and unmelted particles; (d–f) 5 h CMAS corrosion: ridge-like $ZrSiO_4$, amorphous CMAS, and $Zr_xTa_{1-x}O_3$ nanoparticles; and (g–i) 8 h exposure (coarsened features). Gaussian-fitted ridge-like precipitate dimensions after (j) 5 h and (k) 8 h. (l) Log-normal nanoparticle size distribution.

(Fig. 8(d)–8(f)). However, the TKD mapping of the TEM lamella extracted from the ridge-like precipitated phase showed the formation of precipitated phases of monoclinic $ZrSiO_4$ (m-$ZrSiO_4$) (space group: $P2/c$; 13.2 vol%) and tetragonal $ZrSiO_4$ (t-$ZrSiO_4$) (space group: $I4_1/a$; 25.9 vol%), accompanied by a reduction in $Zr_6Ta_2O_{17}$ (11.8 vol%) (Figs. 8(g)–8(i)). This differs from the amorphous phase in the flat CMAS region.

Furthermore, dispersed spherical particles in CMAS exhibited heterogeneous elemental distribution (Fig. 9), supported by the quantitative data in Table 3. After 5 h of corrosion, twin structures formed within CMAS-encapsulated spherical particles. Mg preferentially entered the Ta-rich Zr–Ta–O lattice (Fig. 9(a), area #1), while low-Ta zirconium oxide resisted CMAS penetration (Fig. 9(a), areas #2, #4, and #5). HAADF-STEM confirmed the phase of the twinned spherical zirconia particles, indexed by the $[0\bar{1}1]$ zone axis of m-ZrO_2 with a $(100)_m$ twin boundary (Figs. 10(a)–10(c)). Meanwhile, minimal Zr and Ta diffused into amorphous CMAS in area #3, as indicated in Fig. 9(a). This may suggest that during early corrosion, Mg in CMAS facilitated the decomposition of $Zr_6Ta_2O_{17}$, leading to the precipitation of zirconium oxide and the formation of the Zr–Ta–Mg–O compounds. The defect reaction is described by the Kröger–Vink notation below (Reaction (8)):

$$2MgO + 2Zr_{Zr}^{\times} + 2O_O^{\times} \rightarrow 2Mg_{Zr}^{''} + V_{\ddot{O}} + 2ZrO_2 \quad (8)$$

Prolonged corrosion-induced domain transitions within twinned m-ZrO_2 particles with a domain boundary of $[010]_m||[100]_m$, $(002)_m||(002)_m$ (Figs. 10(d)–10(f)). Moreover, Si incorporation occurred in Ta-rich Zr–Ta–O compounds (Figs. 9(b) and 10(h)), while the Zr–Ta–Mg–Si–O phase in high-tantalum regions retained the o-Ta_2O_5 structure. The atomic-resolution HAADF-STEM images in Figs. 10(g)–10(i) confirm that this structure can be indexed by the [100] axis of o-Ta_2O_5. The black contrast bands formed within the tantalum oxide appear as dislocation-induced lattice kink bands (Fig. 10(i)).

The FIB-lifted TEM lamella from ridge-like precipitates contained dispersed spherical particles embedded in an irregular crystalline matrix with substantially lower o-$Zr_6Ta_2O_{17}$ and o-Ta_2O_5 contents, unlike the phase within the flat area. EDS revealed significant segregation of Si, Ca, Mg, and Al (Fig. 11(a), areas #9 and #10). Selected area electron diffraction and high-resolution TEM (HRTEM) in Figs. 11(b)–11(d) show the

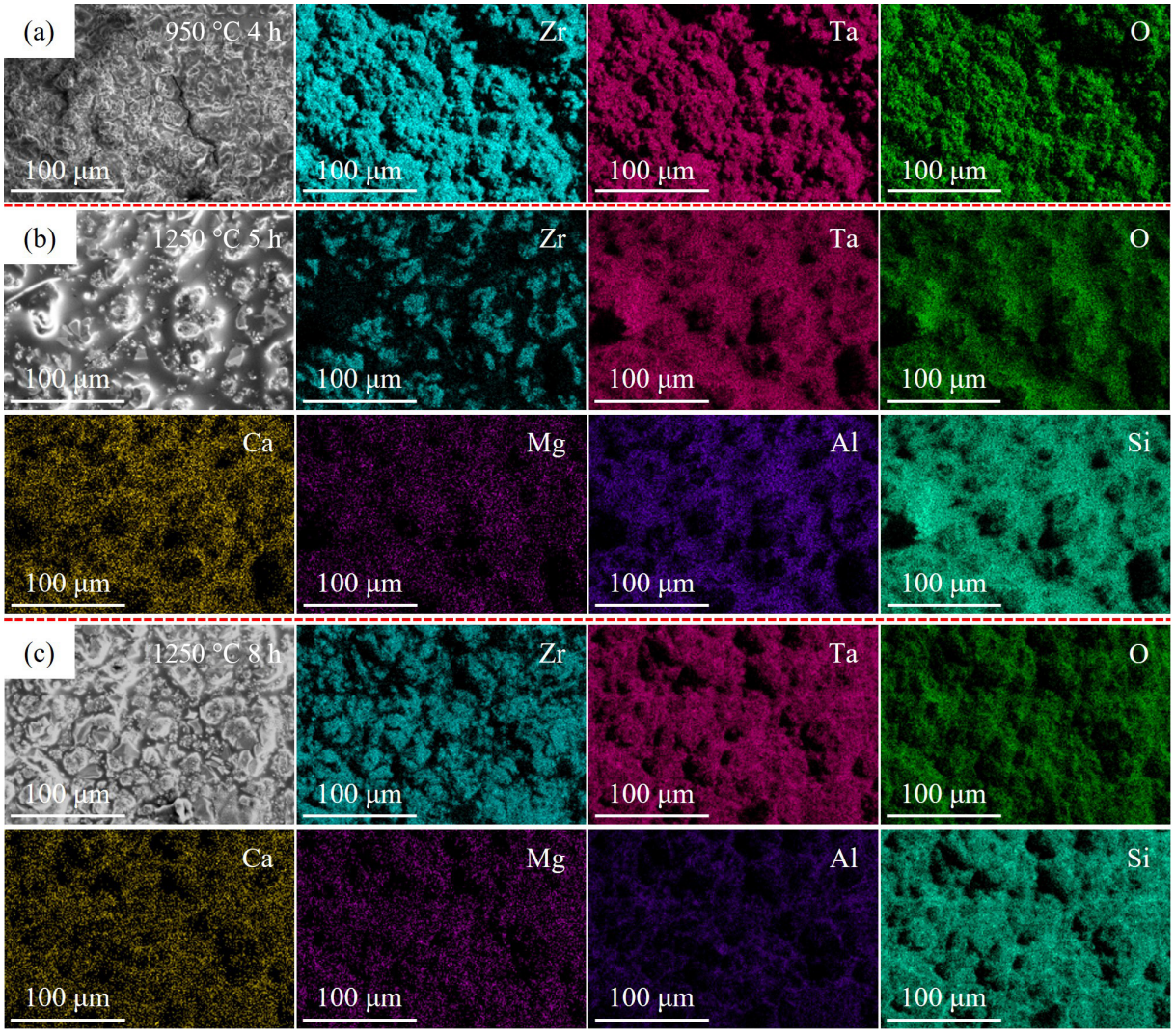

Fig. 4 SEM–EDS images of coating surface at various durations: (a) 950 °C oxygenating for 4 h; (b) 1250 °C CMAS corrosion for 5 h; (c) 1250 °C CMAS corrosion for 8 h.

incomplete decomposition of o-$Zr_6Ta_2O_{17}$ to monoclinic zirconia. The zone axis of o-$Zr_6Ta_2O_{17}$ can be indexed by [011], while the zone axis of m-ZrO_2 can be indexed by [110] with a $(001)_m$ twin interface. The irregular crystalline regions observed in Fig. 11(a) are exclusively composed of $ZrSiO_4$, which is consistent with the phase identification in Figs. 8(g)–8(i). Critically, the global volume fraction of $ZrSiO_4$ quantified by EBSD-TKD statistical analysis reaches 39.1 vol% (Fig. 8(h) annotation).

TEM analysis of the lamellae extracted from the YSZ layer revealed porous microstructures (Fig. 12(a)). The phase structure of the YSZ layer remained unchanged after 5 h of corrosion. Atomic-scale HAADF-STEM confirmed retained t-YSZ, identified with the $[001]_t$ zone axis (Fig. 12(d)). EDS analysis indicates that the pores between the zirconia grains are filled with CMAS. This demonstrates that the sacrificial protection mechanism of the $Zr_6Ta_2O_{17}$ layer can, to a certain extent, protect the integrity of the inner YSZ by isolating the CMAS during attack. After 8 h of CMAS corrosion, severe crack propagation exposed the bonding layer to a high-temperature oxygen environment, triggering rapid growth of uneven TGO that promoted coating cracking and peeling. Atomic-scale HAADF-STEM images near these cracks revealed uncorroded t-ZrO_2 (Figs. 12(b) and 12(e)) and fully oxidized cubic $(Ni_xFe_{1-x})(Cr_yAl_{1-y})_2O_4$ spinel (Figs. 12(c) and 12(f)). This spinel phase underwent accelerated growth that initiated coating cracking.

3.4 Finite element simulation of coating interface stress under CMAS attack

A two-dimensional finite element model (Fig. 13(a)) comprised three domains from top to bottom: Zr–Ta–O coating (1 mm × 25 μm), YSZ coating (1 mm × 25 μm), and substrate (1 mm × 200 μm). Meshing yielded 6932 domain units and 654 boundary units. As shown in Fig. 13(a), CMAS infiltration increased with time at the isothermal corrosion stage, exhibiting a graded distribution with higher penetration near the CMAS source.

After 8 h of isothermal corrosion, the stress contour plot in Fig. 13(b) reveals a temperature-dependent in-plane stress distribution at the cooling stage, while Fig. 13(c) shows the evolution of the in-plane stress within the coating in the direction of penetration with temperature. Initial stresses were minimal, but compressive stress accumulated in the coating domain progressively with prolonged exposure. The in-plane compressive stress accumulated in the YSZ layer notably exceeds the levels in the Zr–Ta–O layer. The maximum compressive stress occurred at

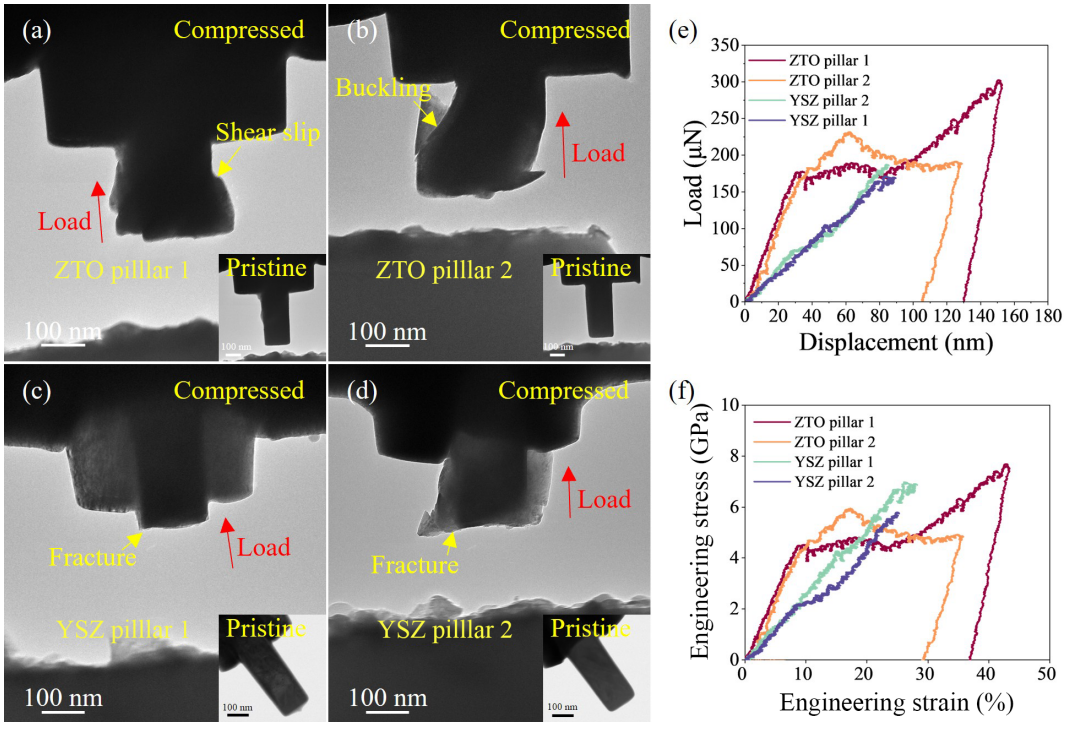

Fig. 5 Comparing compression properties between ZTO core–shell structured pillars and block YSZ pillars via *in situ* near-uniaxial testing. (a, b) Pre- and post-test morphology of ZTO pillars; (c, d) pre-and post-test morphology of YSZ pillars; (e, f) load–displacement and engineering stress–strain curves.

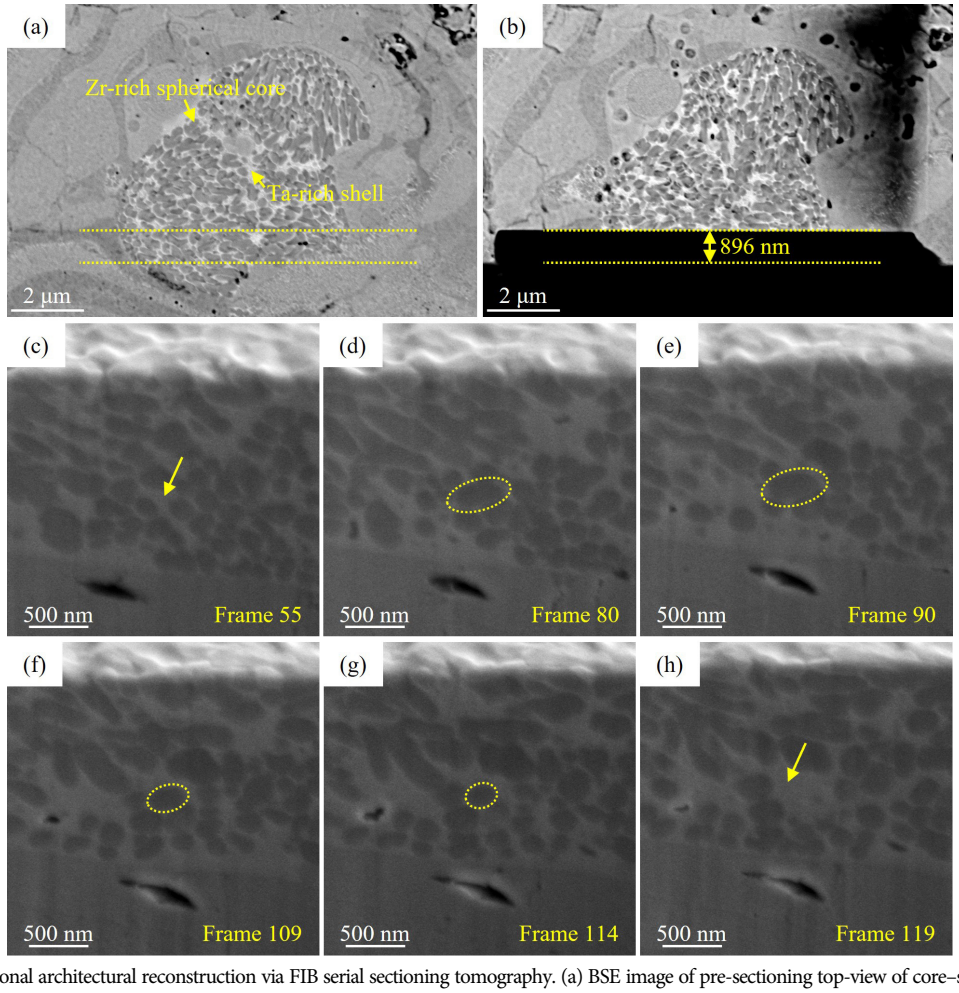

Fig. 6 Three-dimensional architectural reconstruction via FIB serial sectioning tomography. (a) BSE image of pre-sectioning top-view of core–shell structure; (b) BSE image of identical region post-sectioning; (c–h) progressive cross-sectional profiles revealing depth-resolved core–shell evolution during sequential FIB milling.

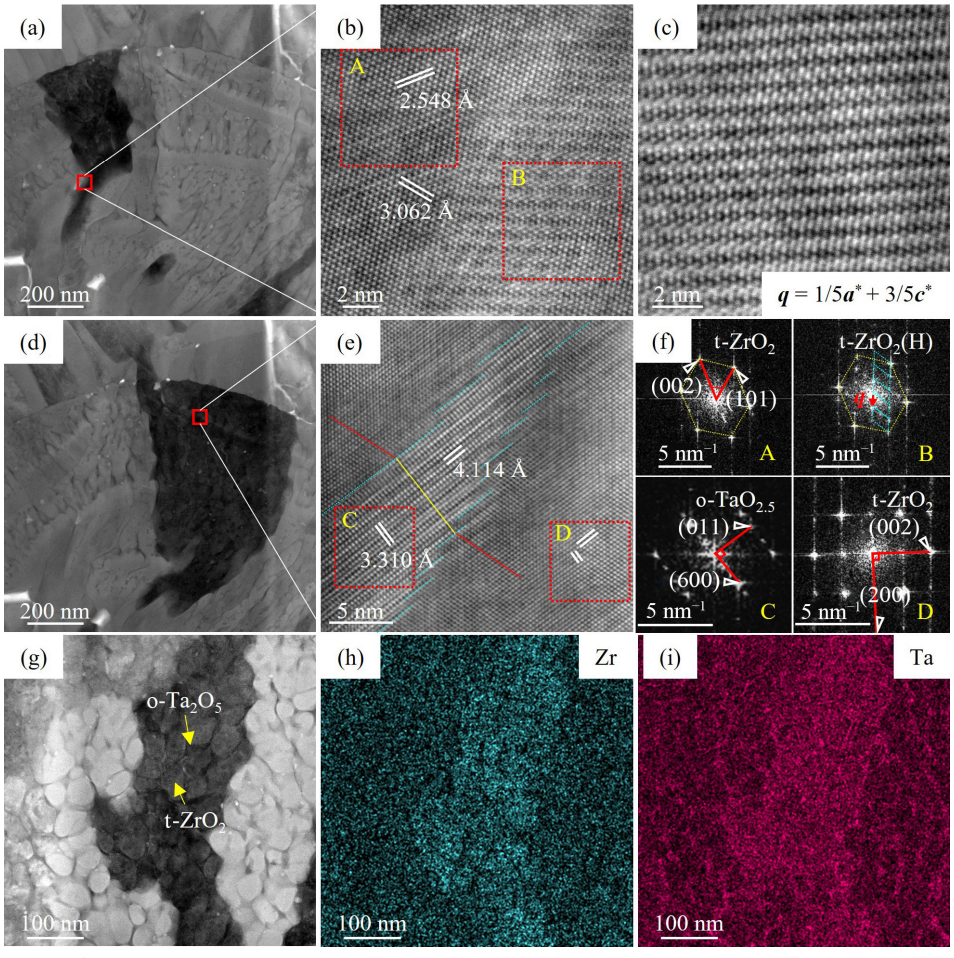

Fig. 7 Microstructure analysis of as-sprayed dense Zr–Ta–O topcoat: (a–c) HAADF-STEM images reveal t-ZrO_2 matrix and superstructure with modulation vector $\boldsymbol{q} = 1/5\boldsymbol{a}^* + 3/5\boldsymbol{c}^*$. (d, e) Droplet-like ZrO_2 particles embedded in a Ta_2O_5-based matrix. (f) FFT patterns from red-dashed regions in (b, e). (g–i) EDS mapping confirms Ta enrichment at grain boundaries (Zr : Ta ≈ 3 : 1 atomic ratio).

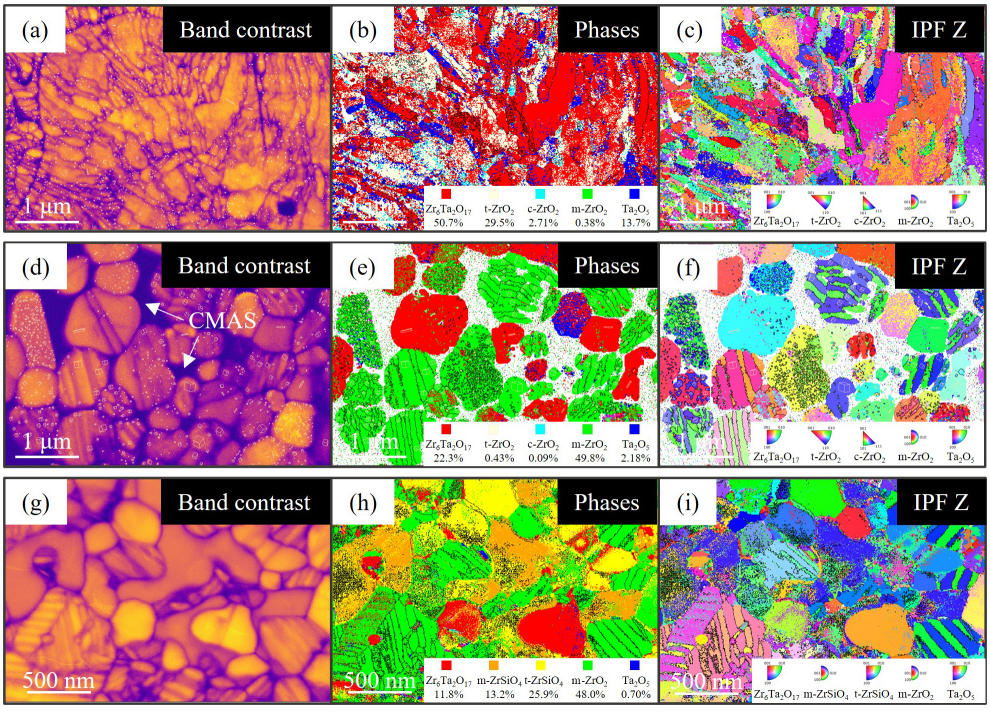

Fig. 8 EBSD-TKD analysis of ZTO coating phases: (a–c) as-oxidized coating: band contrast, phase distribution, and inverse pole figure (IPF) map along *Z*-direction (IPF–Z); (d–f) post-CMAS lamellae lifted out from CMAS area in Fig. 3(i) (1250 °C/8 h): band contrast, phase distribution, and IPF–Z; (g–i) post-CMAS lamellae lifted out from ridge-like area (1250 °C/8 h): band contrast, phase distribution, and IPF–Z.

Table 3 EDS elemental quantification (at%) of different microstructures

Area	Zr–L	Ta–M	Y–L	O–K	Ca–K	Mg–K	Al–K	Si–K	Possible phase
#1	15.19±1.93	11.8±1.50	1.92±0.28	57.22±2.09	0.87±0.16	9.04±1.69	< 2.60	ND	Zr–Ta–Mg–O
#2	35.61±3.51	4.23±0.68	< 1.60	55.46±3.25	< 1.13	ND	ND	ND	ZrO_2
#3	ND	ND	< 0.07	67.60±2.99	2.28±0.32	< 1.00	8.14±1.52	20.91±3.22	CMAS
#4	28.18±2.59	2.88±0.41	0.90±0.13	66.69±2.45	0.21±0.04	< 0.75	< 0.38	ND	ZrO_2
#5	24.41±2.38	3.25±0.45	ND	69.08±2.25	0.69±0.11	1.89±0.40	< 0.68	ND	ZrO_2
#6	6.47±1.09	8.02±1.06	2.67±0.35	61.36±2.08	0.99±0.17	7.76±1.47	1.39±0.34	11.34±2.14	Ta_2O_5
#7	31.61±2.75	3.32±0.47	ND	57.61±2.41	0.71±0.11	< 1.4	< 0.27	< 5	ZrO_2
#8	ND	ND	ND	68.17±3.29	1.52±0.23	ND	6.42±1.24	23.26±3.54	CMAS
#9	32.47±2.76	3.01±0.42	ND	60.20±2.49	0.39±0.06	2.48±0.49	1.46±0.29	ND	$Zr_6Ta_2O_{17}$+ZrO_2
#10	16.17±1.80	ND	ND	62.88±2.69	0.06±0.01	< 0.86	< 0.68	19.36±3.05	$ZrSiO_4$
#11	38.67±2.97	0.05±0.01	1.58±0.22	59.14±2.87	0.12±0.02	0.10±0.02	0.23±0.05	0.11±0.05	ZrO_2
#12	38.76±2.99	0.27±0.04	6.58±0.83	52.95±2.61	0.55±0.08	0.39±0.06	0.36±0.07	0.14±0.02	ZrO_2
#13	0.07±0.01	0.05±0.01	0.02±0.00	64.92±1.88	13.25±1.51	16.70±1.88	2.98±0.58	2.01±0.27	Cr–Ni–Al–Fe–O

Note: When the error is between 20% and 50%, only the upper limit of the data is reported. When the data error exceeds 50%, the "not detected (ND)" mark is used.

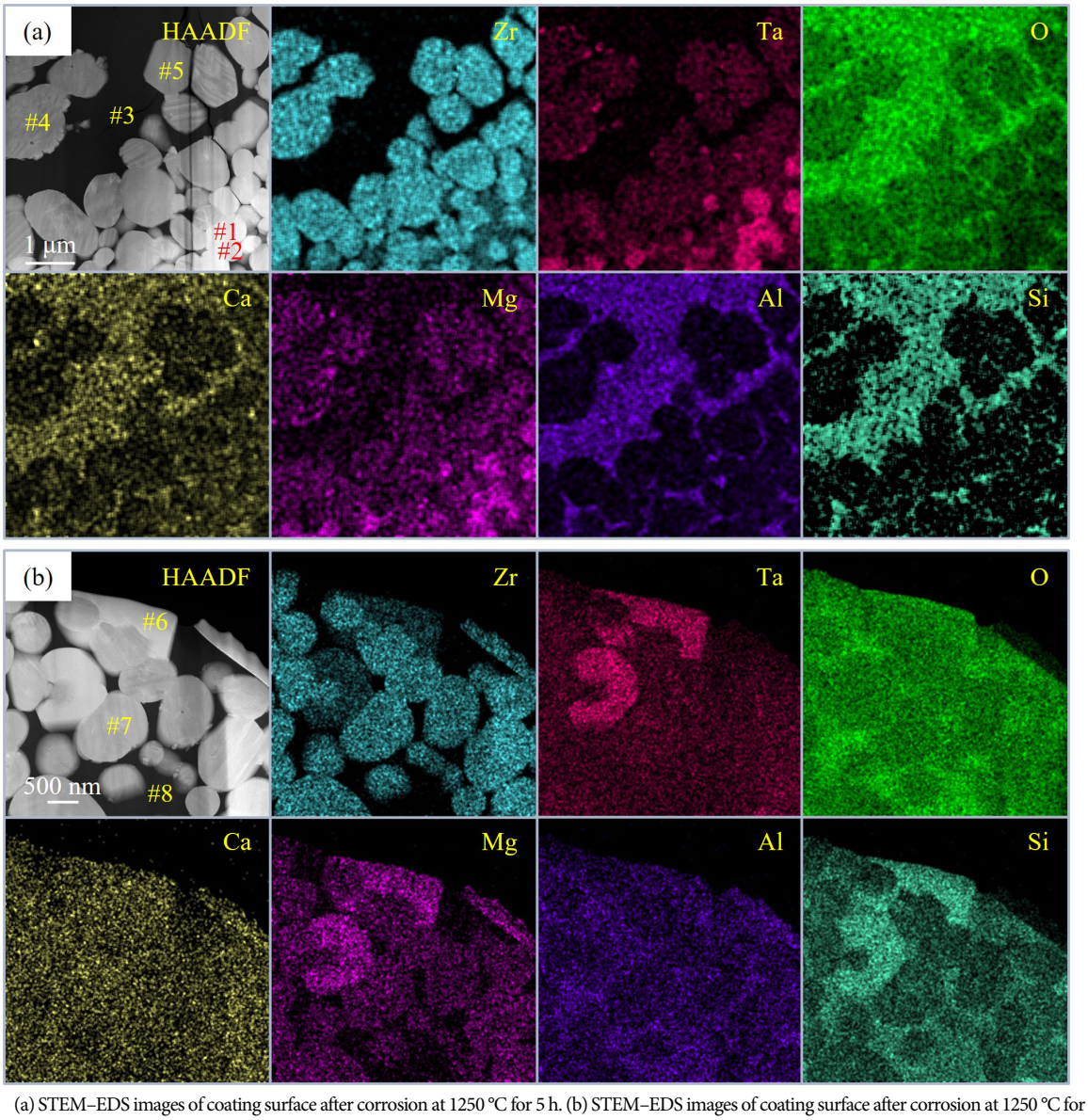

Fig. 9 (a) STEM–EDS images of coating surface after corrosion at 1250 °C for 5 h. (b) STEM–EDS images of coating surface after corrosion at 1250 °C for 8 h.

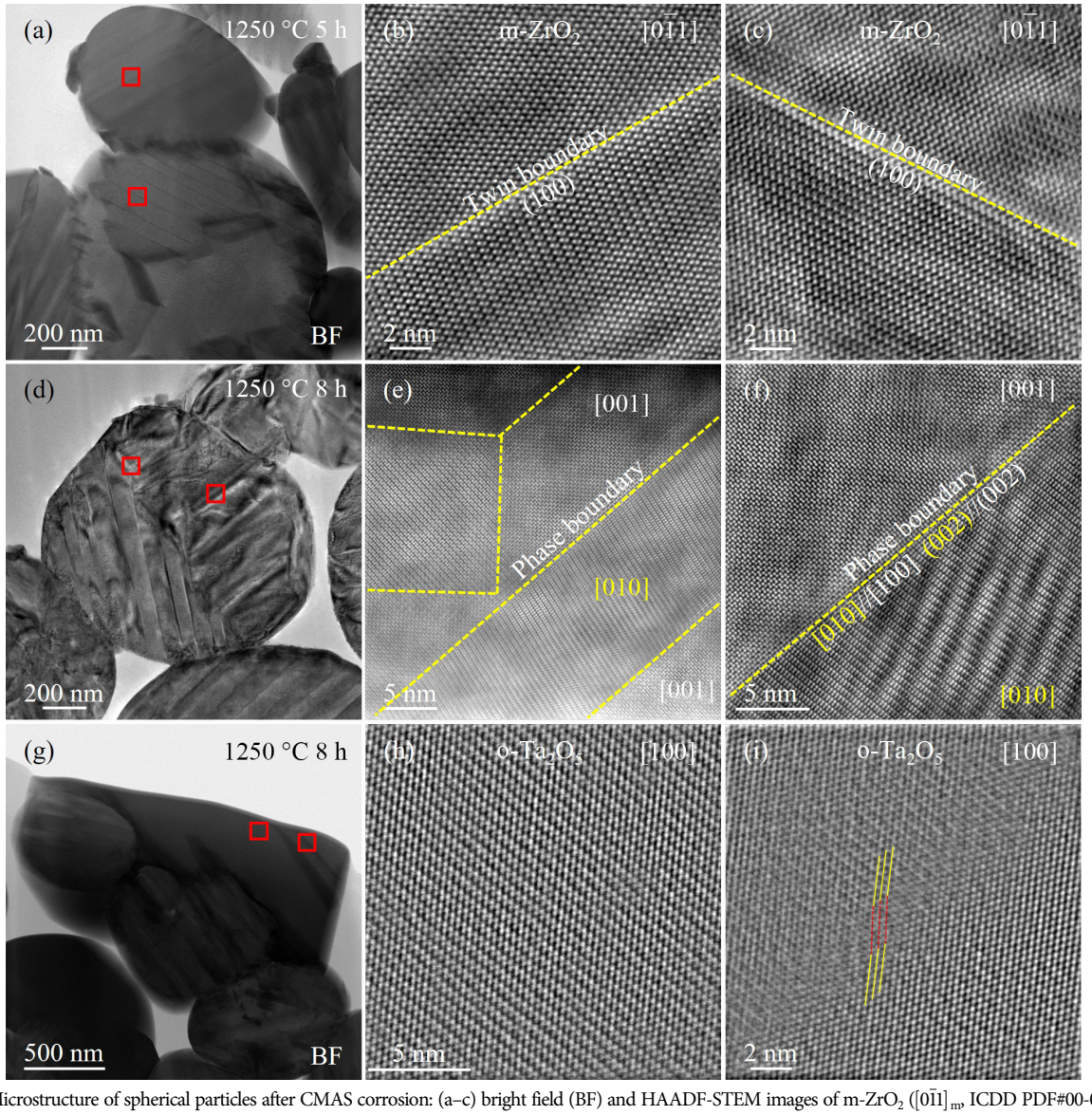

Fig. 10 Microstructure of spherical particles after CMAS corrosion: (a–c) bright field (BF) and HAADF-STEM images of m-ZrO_2 ($[0\bar{1}1]_m$, ICDD PDF#00-036-0420) showing $(100)_m$ twin boundary (1250 °C/5 h); (d–f) TEM and high-resolution STEM (HRSTEM) images of m-ZrO_2 indexed with $[001]_m$ and $[010]_m$, showing twin and phase boundaries (1250 °C/8 h). (g–i) BF and HRSTEM images of o-Ta_2O_5 ($[100]_o$, ICDD PDF#00-054-0514).

the YSZ/substrate interface, indicating a high cracking risk. In addition, the Zr–Ta–O layer exhibited near-surface in-plane compressive stress concentration (Fig. 13(c)). The value of in-plane compressive stress accumulated closer to the top of the Zr–Ta–O layer is greater, suggesting potential layer-by-layer delamination progression.

As shown in Fig. 13(d), the temporal evolution of stress at different infiltration depths within the coating is extracted. It can be observed that with increasing cooling time, the magnitude of the in-plane compressive stress gradually increases. This behavior is primarily attributed to thermally induced mismatch deformation, which becomes more pronounced as the temperature decreases. In addition, a distinct stress jump is observed at approximately 100 min, where the stress magnitude increases abruptly. This is because the system temperature reaches the critical tetragonal-to-monoclinic transformation temperature of fully corroded ZrO_2 at this time, leading to a complete phase transformation in the dissolved regions and the sudden introduction of transformation-induced strain. After the phase transformation is completed, the in-plane compressive stress continues to increase as the temperature further decreases due to the continued intensification of thermal mismatch deformation. Furthermore, the magnitude of the stress jump decreases with increasing infiltration depth. This is attributed to the reduced extent of CMAS-induced corrosion in deeper regions, resulting in a smaller volume fraction of material undergoing phase transformation and, consequently, a reduced contribution from transformation-induced strain.

Ultimately, under the combined effects of phase transformation and thermal mismatch deformation, the accumulated in-plane compressive stress leads to progressive layer-by-layer spallation of the coating.

4 Discussion

4.1 Formation of eutectic microstructure and its strength–toughness coupling mechanisms

Enhancing CMAS resistance in TBCs requires balancing the corrosion limitations of conventional YSZ with the fracture

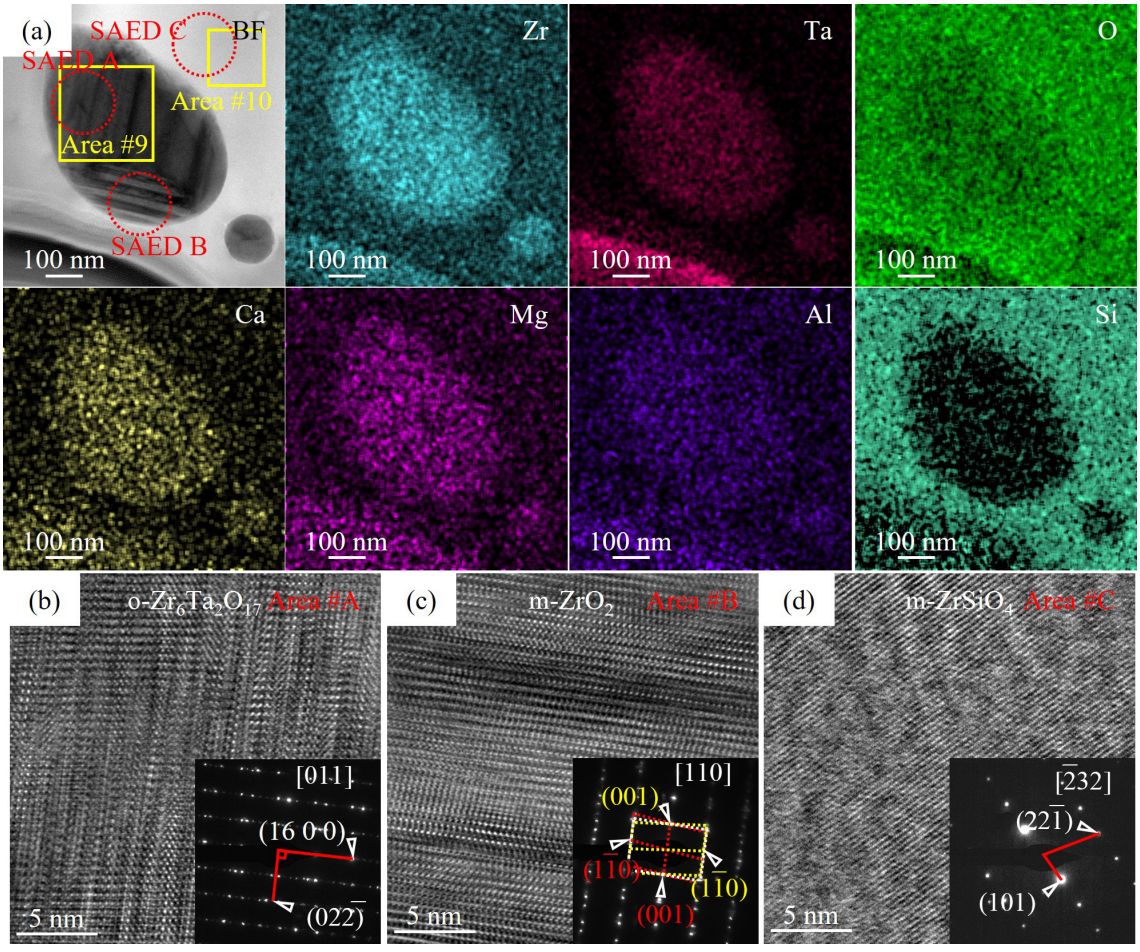

Fig. 11 Microstructure of ridge-like precipitates after 1250 °C/8 h CMAS corrosion: (a) EDS quantification showing CMAS (Ca–Mg–Al) infiltration into globular domains within Zr–Si–O matrix (Table 3). (b–d) HRTEM of regions marked by red-dashed circles in (a): o-$Zr_6Ta_2O_{17}$ ([011]), m-ZrO_2 ([110]), and m-$ZrSiO_4$ ([$\bar{2}$32]).

toughness constraints of new TBC materials. The Zr–Ta–O system offers competitive fracture toughness with that of YSZ [7]. We developed a bilayer coating by utilizing the excellent mechanical properties and high CMAS resistance of the Zr–Ta–O eutectic microstructure, along with the low thermal conductivity, high thermal expansion coefficient, and excellent thermal shock resistance of 8YSZ. APS processing achieved ultradensification (2.0% porosity) while forming a distinctive eutectic core–shell nanoarchitecture through rapid solidification. This process is governed by a metastable peritectic transformation (Reaction (9)) [21]:

$$Zr_6Ta_2O_{17}(\text{orthorhombic}) \rightleftharpoons ZrO_2(\text{ tetragonal }) + L(Zr, Ta, O) \quad (9)$$

Plasma spraying triggers peritectic transformation in $Zr_6Ta_2O_{17}$ feedstock by exceeding its transition temperature, producing coexisting high-temperature tetragonal ZrO_2 (melting point: 2370 °C [11]) and liquid Zr–Ta–O phase. Subsequent cooling drives the nonequilibrium phase decomposition of Ta segregation precipitates orthorhombic Ta_2O_5 (melting point: 1872 °C) [24], creating dense core–shell eutectic structures with spherical t-ZrO_2 cores enveloped by o-Ta_2O_5 shells (Fig. 7). As the peritectic transformation occurs through elemental segregation and reorientation of oxygen coordination polyhedra along specific crystallographic directions [21], the precipitated Ta_2O_5 forms a coherent interface with the ZrO_2 core (Fig. 7(e)).

Mechanical superiority arises from three synergistic mechanisms: (i) coherent o-Ta_2O_5/t-ZrO_2 interface-mediated plasticity (Fig. 7(e)). The atomically matched $(200)_o||(101)_t$, $[01\bar{1}]_o||[010]_t$ facilitates a low-energy pathway for shear glide (> 30% compressive strain in Fig. 5) and a potential crack deflection at shell–core boundaries. (ii) The intragranular t-ZrO_2 superstructure with a modulation vector $\boldsymbol{q} = 1/5\boldsymbol{a}^* + 3/5\boldsymbol{c}^*$ on $(010)_t$ (Figs. 7(b) and 7(f)) accommodates lattice distortion via modulation strain buffering. (iii) o-Ta_2O_5 shells constrain the t-ZrO_2 core, enabling nanoconfinement strengthening that achieves a 4.5 GPa yield strength with retained ductility (Fig. 5(f)). This core–shell eutectic design establishes a new paradigm for damage-tolerant structural ceramics for high-strength and high-deformation applications (e.g., coating of turbine blades).

4.2 CMAS corrosion behavior of eutectic ZTO core–shell layer

Advanced TBCs that resist CMAS primarily rely on either rapid reactive crystallization or promoted self-crystallization of CMAS, which effectively blocks melt infiltration through dense reaction barriers [6]. Eutectic oxide ceramics—notable for their low density, high specific strength, and thermal stability—have garnered significant attention in structural applications such as TBCs and ceramic matrix composites (CMCs) [29]. For Zr–Ta–O eutectics (phases: $Zr_6Ta_2O_{17}$, t-ZrO_2, and o-Ta_2O_5; Figs. 8(a)–8(c)), corrosion triggers $ZrSiO_4$ precipitation through outward Zr^{4+} diffusion into CMAS (evidenced by decreased Zr : Ta ratios and eutectic coarsening; Figs. 8 and 9), in contrast to Song *et al.* [11], who proposed that t-ZrO_2 acts as a host for the $ZrSiO_4$ formation

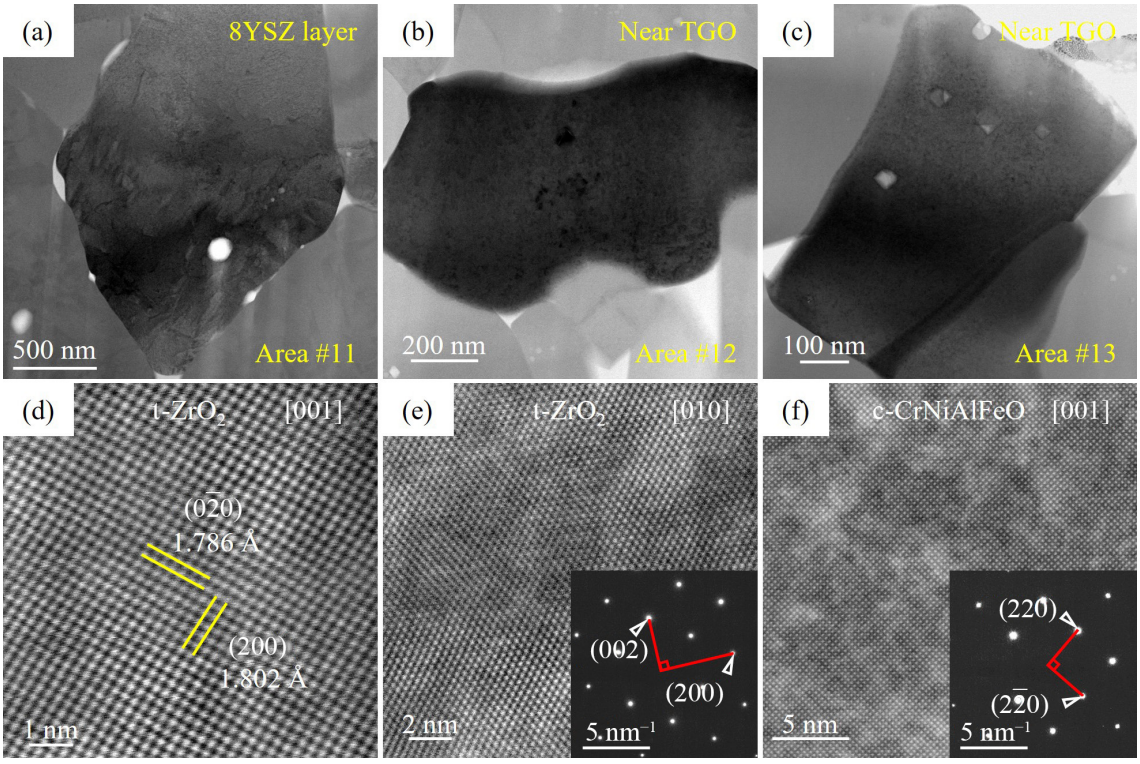

Fig. 12 Phase analysis beneath Zr–Ta–O layer after 1250 °C CMAS corrosion: (a) YSZ layer (5 h); (b) t-ZrO_2 ([010]) near TGO (8 h); (c) $(Ni_xFe_{1-x})(Cr_yAl_{1-y})_2O_4$ ([001], $Fd\bar{3}m$, 8 h); (d–f) corresponding HAADF-STEM.

mechanism. This is analogous to Hf^{4+} diffusion in HfO_2-based systems observed by Cheng *et al.* [25], where Hf substitution for the Si site exhibits a low solution energy (2.61 eV). Furthermore, Mg^{2+} exhibits preferential diffusion into the Zr–Ta–O lattice, forming Zr–Mg–Ta–O compounds (Fig. 9(b)), consistent with the findings of Cheng *et al.* [25] on preferential Ca/Mg mobility [25]. The continuous growth of crystalline phases such as $ZrSiO_4$—which exhibits high thermal stability and a relatively high melting point (1673 °C [40])—significantly enhances the oxidation resistance and thermal stability of the coating [11,41]. To a certain extent, it helps to slow down molten CMAS flow at 1250 °C [25], thereby limiting the corrosive effect within a defined range. In addition, the stabilizer of Ta in the original $Zr_6Ta_2O_{17}$ and t-ZrO_2 precipitates continuously, which is prone to triggering martensitic phase transformation and eventually forms tantalum-deficient zirconia and zirconium-deficient tantalum oxide. Converting the eutectic structure into zircon involves consuming CMAS, promoting crystallization to mitigate infiltration.

4.3 Sacrificial dense eutectic ZTO layer for enhanced CMAS corrosion

The dense eutectic Zr–Ta–O top layer has a thermal expansion coefficient matching YSZ, mitigating bilayer interfacial stresses [42,43]. However, cooling-induced stresses between the dense Zr–Ta–O eutectic and the porous 8YSZ layer generate vertical cracks (density: ~1.0 cracks·mm^{-1}; Fig. 1(d)). These cracks—terminated above the ZTO/YSZ interface [24]—relieve thermal mismatch stresses and satisfy spallation resistance requirements. Critically, these cracks serve as preferential pathways for CMAS infiltration within the dense ZTO layer (Fig. 2(a)).

Above the CMAS melting temperatures, Zr^{4+} diffusion from the Zr–Ta–O eutectic phase reduces the thermal expansion coefficient of the dense, $ZrSiO_4$-rich reaction layer (Fig. 3). Within this layer, localized t → m martensitic transformations, twinning, and ferroelastic domain switching in t-ZrO_2 enhance toughening—alleviating thermal mismatch strains during thermal shocks (Fig. 8). However, prolonged reaction induced ~3%–5% volume expansion from phase transformations, generating compressive stresses upon cooling that triggered spallation of the infiltrated layer (Figs. 1(g)–1(l)). The simulation results confirm that the compressive stress in the reaction layer progressively increases during rapid cooling (Fig. 13(d)). This sacrificial spallation removes CMAS, minimizing infiltration into the underlying YSZ (Fig. 12(a)) and preventing CMAS penetration near the bond coat (Fig. 2(b)), thereby preserving coating integrity (Fig. 14).

While minor coating spallation remains acceptable under service conditions (protected by backside cooling and adjacent oxides [4]), prolonged corrosion propagates cracks toward the bond coat, accelerating TGO growth. Upon reaching a critical thickness (5.5 μm [44]), TGO-induced stresses trigger YSZ spallation (Fig. 1(k)). Critically, inadequate bond coat Al content promotes nonprotective Cr-rich spinel formation—$(Ni_xFe_{1-x})(Cr_yAl_{1-y})_2O_4$—over protective α-$Al_2O_3$ scales. This accelerates severe oxygen penetration with metallic counterdiffusion [4], generating porous, brittle spinel layers (60.2±12.2 μm; Fig. 1(l)) that degrade oxidation resistance [44].

Therefore, CMAS-induced failure in ZTO/8YSZ bilayer coatings occurs in two stages: (i) CMAS infiltration changes near-surface mechanical properties, leading to reaction layer spallation caused by mismatch strain; (ii) spallation results in the widening of vertical cracks that extend to the bond coat interface. Mismatch stresses from the rapid, uneven growth of spinel or chromia phases trigger subsurface delamination near surface-connected vertical cracks [5], triggering rapid cracking and spallation of the YSZ layer.

To rigorously evaluate our bilayer coating's competitiveness, a parallel CMAS corrosion test at 1250 °C compares three systems: (1) conventional APS YSZ monolayers, (2) electron-beam physical

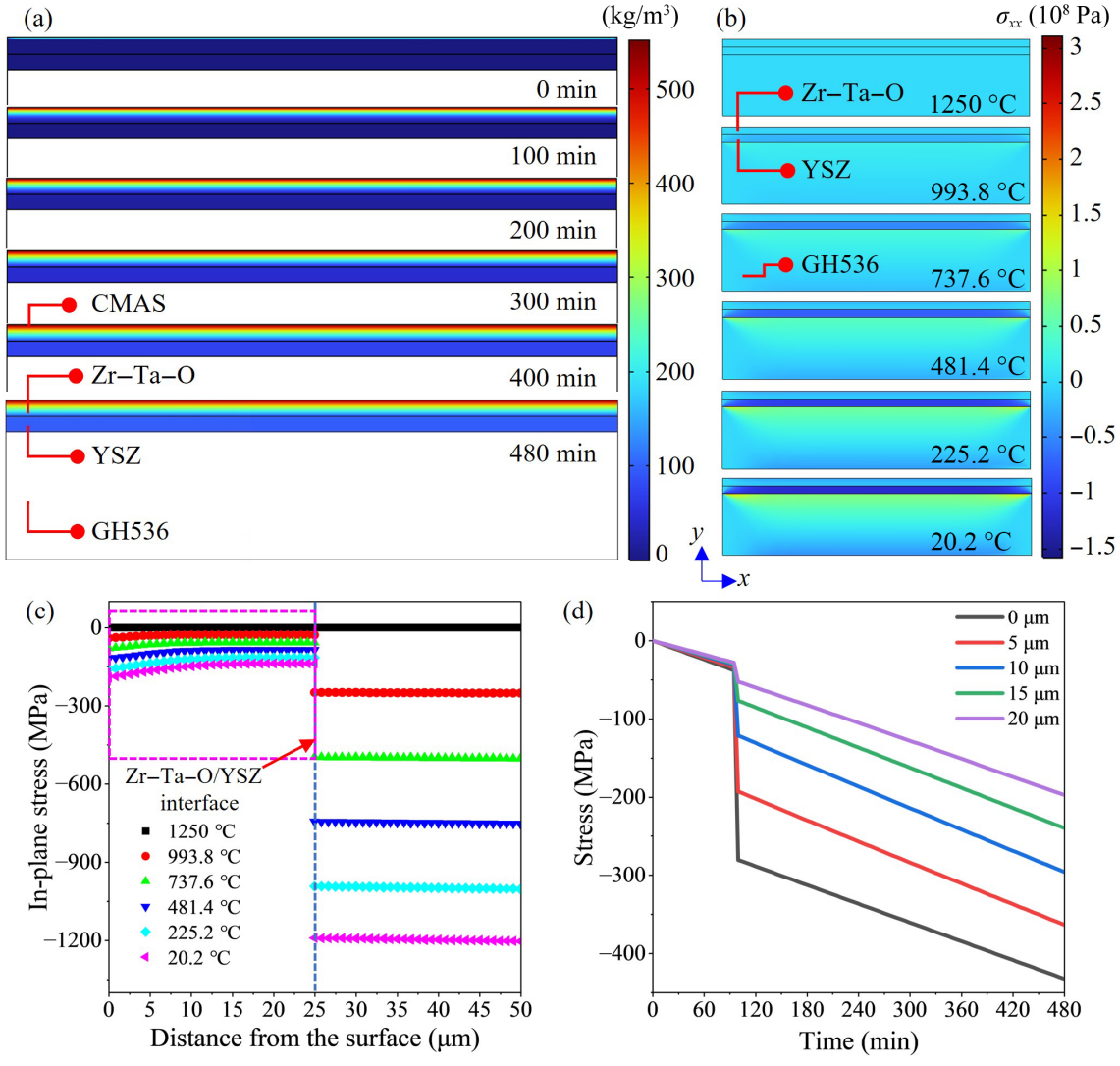

Fig. 13 CMAS corrosion simulation. (a) Time-dependent CMAS penetration distribution at 1250 °C. (b) Stress contour in TBC system during cooling after 8 h of CMAS corrosion at 1250 °C. (c) Evolution of in-plane stress as a function of depth within coating during cooling. (d) Depth-resolved in-plane stress evolution in Zr–Ta–O layer during cooling after CMAS corrosion (1250 °C, 8 h).

vapor deposited (EB-PVD) $La_2Zr_2O_7$/YSZ bilayers, and (3) our designed core–cell ZTO/YSZ bilayer (Figs. S5–S9 in the ESM). APS-YSZ monolayers exhibited minimal resistance, with CMAS penetrating to the substrate within 2 h. Cross-sectional EDS confirmed extensive substrate attack, ultimately triggering macroscopic spallation from thermal mismatch stress (Figs. S5–S7 in the ESM). The EB-PVD $La_2Zr_2O_7$/YSZ bilayer showed better spallation resistance but suffered rapid CMAS infiltration through intercolumnar gaps within 3 h, consuming the $La_2Zr_2O_7$ topcoat and oxidizing the bond coat (Fig. S9(c) in the ESM). Significant YSZ spallation exposed > 50% substrate by 6 h, culminating in near-complete coating depletion at 7 h (Figs. S8(d)–S8(f) in the ESM).

In marked contrast, our eutectic ZTO/YSZ bilayer demonstrated exceptional CMAS resistance under identical conditions (Fig. 1), outperforming rare-earth zirconates through synergistic mechanisms : (1) Dense ZTO impedes initial CMAS wetting. The rapid solidification-induced eutectic densification during the APS spraying process (Fig. 1(a)) forms an ultralow porosity barrier (2.0%) that prevents initial CMAS penetration for over 120 min at 1250 °C. (2) The self-passivating reaction products block further penetration (Fig. 2). Engineered cracks terminating at the ZTO/YSZ interface consume CMAS into $ZrSiO_4$. (3) The exceptional mechanical properties of the eutectic Zr–Ta–O layer: > 30% compressive plasticity (Fig. 5(f)) accommodates thermal stresses, preventing premature cracking during sealing; coherent core–shell interfaces (Fig. 7(e)) maintain a 4.5 GPa strength while enabling slip (Fig. 5(f)); superstructure formation ($\boldsymbol{q}$ = 1/5$\boldsymbol{a}^*$ + 3/5$\boldsymbol{c}^*$) in t-ZrO_2 grains (Figs. 7(a)–7(c)) enhances lattice distortion tolerance. The architecture-designed bilayer systems outperform traditional solutions not only in CMAS durability but also in thermomechanical reliability—significantly advancing next-generation thermal barrier coating paradigms.

While the CMAS resistance was compromised by excessive TGO growth at the bond coat interface (Figs. 1(k) and 1(l)), a limitation of this study is the discrepancy between the experimental conditions and real TBC service environments, requiring further validation under more practical conditions. However, furnace holding acts as an accelerated corrosion test that often causes overoxidation, demanding higher requirements for bond coat and substrate treatment. Bond coats require sufficient Al to form protective α-Al_2O_3 scales during initial oxidation, limiting TGO thickness and reducing in-plane stresses—unlike

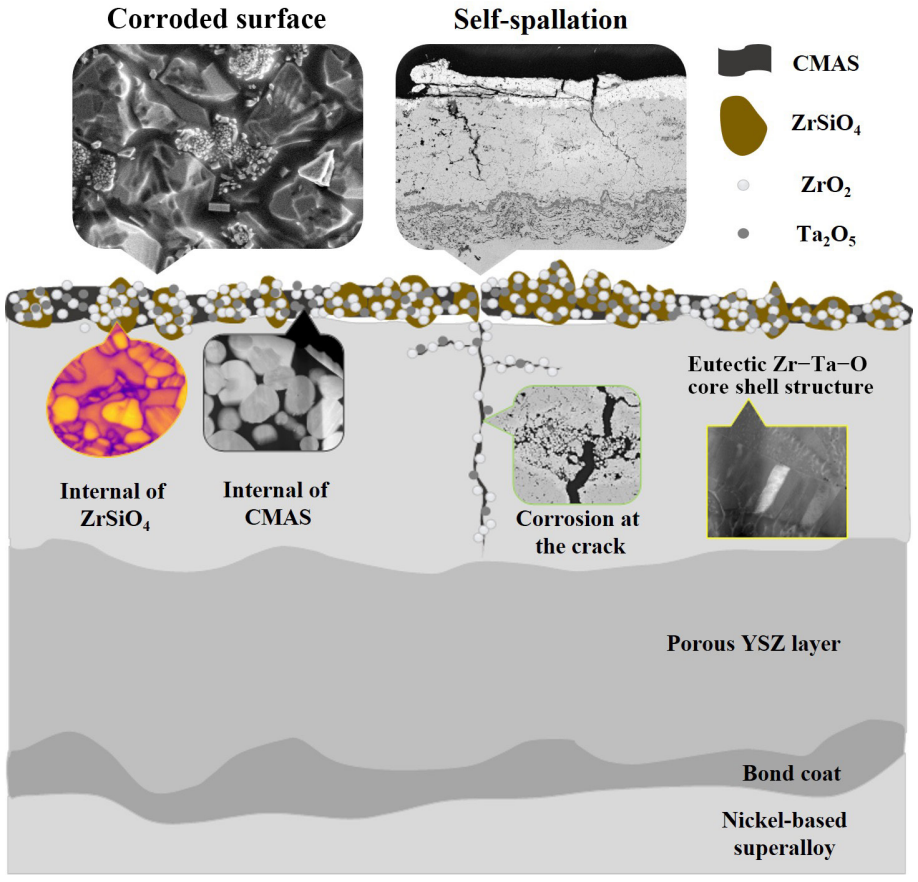

Fig. 14 Schematic diagram of sacrificial reaction mechanism of dense ZTO eutectic core–shell structure through sealing, consuming, and self-spalling during CMAS attack.

the chromia or spinel structures observed in Refs. [4,24]. Current limitations arise from TGO-induced delamination at the bond coat, not the sacrificial mechanism itself. Future efforts should (i) develop TGO-resistant bond coats (e.g., Pt-diffusion modified NiAl) compatible with ZTO/8YSZ; (ii) optimize spallation kinetics via shell thickness control (3–13 nm in Fig. 7(e)) to synchronize with CMAS attack rates; and (iii) implement laser-assisted recoating for sacrificial layer renewal.

5 Conclusions

This work introduces a bilayer TBC system via APS deposition, featuring a eutectic Zr–Ta–O core–shell top layer over a YSZ underlayer. The design pioneers sacrificial protection: Densified growth of the eutectic Zr–Ta–O core–shell layer seals against CMAS infiltration, surface-precipitated ZrO_2 forms zircon barriers to immobilize corrosive species, and thermal shock-induced spallation self-removes infiltrated zones. The top layer demonstrates superior compressive properties (over 30% plastic strain, ~4.5 GPa yield strength), meeting TBC mechanical requirements. CMAS-induced delamination causes vertical cracking under thermal shock, which spalls entire infiltrated zones, quickly isolating corrosion to protect YSZ. The architected dense-eutectic ZTO/YSZ bilayer coating design delivers superior CMAS resistance by integrating dual structural functions: intrinsic self-sealing of the ZTO top layer against melt infiltration and engineered self-removal sacrifice during thermal cycling.

Acknowledgements

We acknowledge the Instrumental Analysis Center of Xidian University.

Author contributions

Jun-Hui Luo: conceptualization, validation, formal analysis, investigation, writing – original draft, and writing – review and editing. Gang Yan: writing – review and editing. Guang-Nan Xu: methodology, investigation, writing – review and editing, formal analysis, and visualization. Chang-Xing Zhang: investigation, writing – review and editing, and formal analysis. Ke Cao: writing – review and editing, investigation, supervision, and funding acquisition. Jun-Kai Liu: writing – review and editing. Yi-Chun Zhou: supervision, funding acquisition. Li Yang: writing – review and editing, resources, supervision, and funding acquisition.

Availability of data and materials

The data that support the findings of this study are available from the corresponding author upon reasonable request.

Competing interests

The authors have no competing interests to declare that are relevant to the content of this article.

Electronic Supplementary Material

Supplementary materials (Movies 1–5) are available in the online version of this article at https://doi.org/10.26599/JAC.2026.9221300.

Funding

This work was supported by the National Natural Science Foundation of China (Nos. 92371204, 12202330, 12502208 (PI: Qian-Qian Zhou), and U2341257), the National Science and

Technology Major Project (No. J2022-V-0003-0029), the Fundamental Research Funds for the Central Universities and the Innovation Fund of Xidian University (No. YJSJ25017).

References

[1] Padture NP. Advanced structural ceramics in aerospace propulsion. *Nat Mater* 2016, **15**: 804–809.

[2] Darolia R. Thermal barrier coatings technology: Critical review, progress update, remaining challenges and prospects. *Int Mater Rev* 2013, **58**: 315–348.

[3] Padture NP, Gell M, Jordan EH. Thermal barrier coatings for gas-turbine engine applications. *Science* 2002, **296**: 280–284.

[4] Evans AG, Clarke DR, Levi CG. The influence of oxides on the performance of advanced gas turbines. *J Eur Ceram Soc* 2008, **28**: 1405–1419.

[5] Mercer C, Faulhaber S, Evans AG, *et al.* A delamination mechanism for thermal barrier coatings subject to calcium–magnesium–alumino–silicate (CMAS) infiltration. *Acta Mater* 2005, **53**: 1029–1039.

[6] Liu S, Hu XP, Liu Q, *et al.* Effect of HfO_2 content on CMAS corrosion resistance of a promising $Hf_6Ta_2O_{17}$ ceramic for thermal barrier coatings. *Corros Sci* 2022, **208**: 110712.

[7] Liu Q, Hu XP, Zhu W, *et al.* Effects of Ta_2O_5 content on mechanical properties and high-temperature performance of $Zr_6Ta_2O_{17}$ thermal barrier coatings. *J Am Ceram Soc* 2021, **104**: 6533–6544.

[8] Wu D, Yao Y, Shan X, *et al.* Equimolar $YO_{1.5}$ and $TaO_{2.5}$ co-doped ZrO_2 as a potential CMAS-resistant material for thermal barrier coatings. *J Am Ceram Soc* 2021, **104**: 1132–1145.

[9] Xu ZH, He LM, Mu RD, *et al.* Double-ceramic-layer thermal barrier coatings of $La_2Zr_2O_7$/YSZ deposited by electron beam-physical vapor deposition. *J Alloy Compd* 2009, **473**: 509–515.

[10] Zhuo XS, Sun XM, Wu J, *et al.* Molten CMAS resistance strategy for PS-PVD TBCs based on laser textured and Al-modified bionic structure. *npj Mat Degrad* 2024, **8**: 85.

[11] Song KQ, Fan JL, Li W, *et al.* Effect of ZrO_2 types on $ZrSiO_4$ formation. *Ceram Int* 2019, **45**: 23444–23450.

[12] Wu Y, Zhi WB, Li Y, *et al.* Interactions between rare-earth zirconates ($RE_2Zr_2O_7$) and CMAS silicate melts. *Corros Sci* 2023, **224**: 111526.

[13] Feng J, Shian S, Xiao B, *et al.* First-principles calculations of the high-temperature phase transformation in yttrium tantalate. *Phys Rev B* 2014, **90**: 094102.

[14] Luo C, Li C, Cao K, *et al.* Ferroelastic domain identification and toughening mechanism for yttrium tantalate–zirconium oxide. *J Mater Sci Technol* 2022, **127**: 78–88.

[15] Guo L, Li G, Gan ZL. Effects of surface roughness on CMAS corrosion behavior for thermal barrier coating applications. *J Adv Ceram* 2021, **10**: 472–481.

[16] Han Y, Liu XY, Zhang QQ, *et al.* Ultra-dense dislocations stabilized in high entropy oxide ceramics. *Nat Commun* 2022, **13**: 2871.

[17] Xiang HM, Xing Y, Dai FZ, *et al.* High-entropy ceramics: Present status, challenges, and a look forward. *J Adv Ceram* 2021, **10**: 385–441.

[18] Voskanyan AA, Lilova K, McCormack SJ, *et al.* A new class of entropy stabilized oxides: Commensurately modulated $A_6B_2O_{17}$ (A = Zr, Hf; B = Nb, Ta) structures. *Scripta Mater* 2021, **204**: 114139.

[19] McCormack SJ, Tseng KP, Weber RJK, *et al. In-situ* determination of the HfO_2–Ta_2O_5-temperature phase diagram up to 3000 °C. *J Am Ceram Soc* 2019, **102**: 4848–4861.

[20] Tan ZY, Xie ZH, Wu X, *et al.* Spark plasma sintering of $A_6B_2O_{17}$ (A = Hf, Zr; B = Ta, Nb) high entropy ceramics. *Mater Lett* 2023, **330**: 133381.

[21] McCormack SJ, Weber RJ, Kriven WM. *In-situ* investigation of $Hf_6Ta_2O_{17}$ anisotropic thermal expansion and topotactic, peritectic transformation. *Acta Mater* 2018, **161**: 127–137.

[22] Tan ZY, Yan G, Cao K, *et al.* Effect of microstructure on the performance of $Zr_6Ta_2O_{17}$ ceramics as thermal barrier coatings. *Ceram Int* 2023, **49**: 29449–29458.

[23] Li M, Xu Q, Wang L. High-temperature chemical stability of $Hf_6Ta_2O_{17}$ ceramic for thermal barrier coatings. *Key Eng Mater* 2012, **512–515**: 635–638.

[24] Sun Y, Wu X, Tan ZY, *et al.* Boosting the strain tolerance of Ta_2O_5 stabilized ZrO_2 TBCs through prefabricated cracks by *in-situ* reaction. *J Alloy Compd* 2023, **935**: 168131.

[25] Cheng CY, Chen L, Luo JH, *et al.* Initial corrosion mechanism of $Hf_6Ta_2O_{17}$ ceramic for TBCs against CMAS infiltration: Experiment and first-principle simulation. *Corros Sci* 2023, **225**: 111626.

[26] Tan ZY, Yang ZH, Zhu W, *et al.* Mechanical properties and calcium–magnesium–alumino–silicate (CMAS) corrosion behavior of a promising $Hf_6Ta_2O_{17}$ ceramic for thermal barrier coatings. *Ceram Int* 2020, **46**: 25242–25248.

[27] Tan ZY, Pan TT, Nie M, *et al.* Exceptional hot corrosion resistance behavior and mechanism of double layered $Zr_6Ta_2O_{17}$/YSZ thermal barrier coatings exposed to Na_2SO_4–V_2O_5 salt. *Corros Sci* 2025, **246**: 112761.

[28] Feng WB, Sun Y, Fan CF, *et al.* The enhanced mechanical properties for $Hf_6Ta_2O_{17}$ thin film through component segregation. *Thin Solid Films* 2024, **799**: 140408.

[29] Li H, Yu YP, Fang B, *et al.* $Hf_6Ta_2O_{17}$/Ta_2O_5 composite ceramic: A new eutectic system. *Ceram Int* 2022, **48**: 13516–13523.

[30] Tan ZY, Wu X, Guo JW, *et al.* Toughness mechanism and plastic insensitivity of submicron second phase Ta in a novel Ta–$Hf_6Ta_2O_{17}$ composite ceramic. *Ceram Int* 2023, **49**: 1932–1939.

[31] Myers DL, Kulis MJ, Horwath JP, *et al.* Interactions of Ta_2O_5 with water vapor at elevated temperatures. *J Am Ceram Soc* 2017, **100**: 2353–2357.

[32] Zhang J, Wang S, Li W, *et al.* Understanding the oxidation behavior of Ta–Hf–C ternary ceramics at high temperature. *Corros Sci* 2020, **164**: 108348.

[33] Cheng CY, Lv TT, Song BH, *et al.* Thermal cycling property of the novel $Hf_6Ta_2O_{17}$/YSZ TBCs prepared by atmospheric plasma spraying technology. *Surf Interfaces* 2024, **53**: 105050.

[34] Cheng CY, Lv TT, Wu YH, *et al.* Thermal decomposition behavior of $Hf_6Ta_2O_{17}$ powders: Experiment and *ab initio* molecular dynamics simulation. *J Alloy Compd* 2024, **1009**: 176915.

[35] Luo JH, Wang QW, Cao K, *et al.* Unraveling the intrinsic phase evolution mechanisms behind strength and toughness improvements in Y-TZP. *Mat Sci Eng A—Struct* 2025, **946**: 149170.

[36] Xu GN, Yang L, Zhou YC, *et al.* A chemo–thermo-mechanically constitutive theory for thermal barrier coatings under CMAS infiltration and corrosion. *J Mech Phys Solids* 2019, **133**: 103710.

[37] Zhang GH, Fan XL, Xu R, *et al.* Transient thermal stress due to the penetration of calcium–magnesium–alumino–silicate in EB-PVD thermal barrier coating system. *Ceram Int* 2018, **44**: 12655–12663.

[38] Abubakar AA, Akhtar SS, Arif AFM. Phase field modeling of V_2O_5 hot corrosion kinetics in thermal barrier coatings. *Comp Mater Sci* 2015, **99**: 105–116.

[39] Garces HF, Senturk BS, Padture NP. *In situ* Raman spectroscopy studies of high-temperature degradation of thermal barrier coatings by molten silicate deposits. *Scripta Mater* 2014, **76**: 29–32.

[40] Hu Y, Lu J, Ni DW, *et al.* Microstructure evolution and ablation mechanisms of C_{sf}/ZrB_2–SiC composites at different heat fluxes under air plasma flame. *J Eur Ceram Soc* 2024, **44**: 3514–3524.

[41] Gao D, Zhang Y, Fu JY, *et al.* Oxidation of zirconium diboride–silicon carbide ceramics under an oxygen partial pressure of 200 Pa: Formation of zircon. *Corros Sci* 2010, **52**: 3297–3303.

[42] Liu Q, Hu XP, Zhu W, *et al.* Thermal shock performance and failure behavior of $Zr_6Ta_2O_{17}$–8YSZ double-ceramic-layer thermal barrier coatings prepared by atmospheric plasma spraying. *Ceram Int* 2022, **48**: 24402–24410.

[43] Hayashi H, Saitou T, Maruyama N, *et al.* Thermal expansion coefficient of yttria stabilized zirconia for various yttria contents. *Solid State Ionics* 2005, **176**: 613–619.

[44] Li Y, Li CJ, Zhang Q, *et al.* Influence of TGO composition on the thermal shock lifetime of thermal barrier coatings with cold-sprayed MCrAlY bond coat. *J Therm Spray Techn* 2010, **19**: 168–177.